

Quantum circuit and mapping algorithms for wavepacket dynamics: case study of anharmonic hydrogen bonds in protonated and hydroxide water clusters

Debadrita Saha,

*Department of Chemistry, and the Indiana University Quantum Science and Engineering Center (IU-QSEC),
Indiana University, 800 E. Kirkwood Ave, Bloomington, IN-47405*

Philip Richerme

Department of Physics, and the Indiana University Quantum Science and Engineering Center (IU-QSEC), Indiana University, Bloomington, IN-47405

Srinivasan S. Iyengar,

*Department of Chemistry, Department of Physics,
and the Indiana University Quantum Science and Engineering Center (IU-QSEC),
Indiana University, 800 E. Kirkwood Ave, Bloomington, IN-47405*

(Dated: December 6, 2024)

The accurate computational study of wavepacket nuclear dynamics is considered to be a classically intractable problem, particularly with increasing dimensions. Here we present two algorithms that, in conjunction with other methods developed by us, will form the basis for performing quantum nuclear dynamics in arbitrary dimensions. For one algorithm, we present a direct map between the Born-Oppenheimer Hamiltonian describing the wavepacket time-evolution and the control parameters of a spin-lattice Hamiltonian that describes the dynamics of qubit states in an ion-trap quantum computer. This map is exact for three qubits, and when implemented, the dynamics of the spin states emulate those of the nuclear wavepacket. However, this map becomes approximate as the number of qubits grow. In a second algorithm we present a general quantum circuit decomposition formalism for such problems using a method called the Quantum Shannon Decomposition. This algorithm is more robust and is exact for any number of qubits, at the cost of increased circuit complexity. The resultant circuit is implemented on IBM's quantum simulator (QASM) for 3-7 qubits. In both cases the wavepacket dynamics is found to be in good agreement with the classical result and the corresponding vibrational frequencies obtained from the wavepacket density time-evolution, are in agreement to within a few tenths of a wavenumbers.

I. INTRODUCTION

Protonated¹⁻³, neutral⁴ and hydroxide-rich water clusters⁵⁻¹⁰ have been widely studied, both experimentally¹¹⁻¹⁵ and theoretically¹⁶⁻¹⁹ due to their broad significance in multiple areas including atmospheric²⁰⁻²², biological²³⁻²⁷ and condensed phase chemistry^{28,29}. There have been substantial efforts devoted to the understanding of the relatively high efficiency of organic reactions on the surface of water droplets³⁰⁻⁴⁸. Protonated water clusters in polymer electrolyte membrane fuel cells⁴⁹ mediate proton transfer.

Experimental studies on vibrational properties of such hydrogen bonded cluster systems have blossomed due to the development of sophisticated cluster-based measurement techniques such as Argon-tagged single photon action spectral methods⁵⁰ and the Infra-red Multiple Photon Dissociation (IRMPD)⁵¹ approach. Both gas phase single-photon^{50,52} and multiple-photon^{51,53-56} vibrational action spectroscopic techniques have been crucial in deciphering the precise signatures that contribute to dynamics and spectroscopy in hydrogen bonded systems. However, the accurate computational modeling of the processes involved in these experiments requires both the quantum mechanical treatment of elec-

tronic as well as nuclear motion. Due to the light mass of the transferring proton involved in such hydrogen bonded systems, these systems often exhibit quantum effects such as hydrogen tunneling and zero-point energy⁵⁷⁻⁶³, and the correlated behavior of multiple nuclear degrees of freedom^{52,64-75}. In such scenarios, classical approaches such as approximating nuclear motion to be harmonic about the equilibrium geometry^{76,77} fail to accurately predict the static and dynamic properties of such hydrogen-bonded systems^{1,52,64,78,79}. A full quantum mechanical treatment of the nuclear degrees of freedom and its associated electronic interactions is often needed^{64,72-74,80,81} to account for such quantum nuclear effects, including multi-dimensional effects, in the computation of their molecular properties. This then requires the computation of potential energy surfaces for describing the nuclear degrees of freedom in such systems, and the explicit time evolution of the quantum nuclear wave packet on the potential landscape. However, the study of such multi-dimensional quantum nuclear processes is complicated by: (a) the steep algebraic computational scaling of accurate electron correlation methods⁸², and (b) the exponential scaling of quantum nuclear dynamics with the number of quantum nuclear degrees of freedom⁸³⁻⁹⁵.

Over the years several classical algorithms have been

developed to improve the computational scaling of electronic^{96–100} and nuclear dynamics^{85,101–105} problems. Orthogonally, recent years have also seen the development of quantum algorithms for performing electronic structure calculations on near-term quantum hardware. Promising quantum algorithms^{106–116} and experiments^{117–123} that address systems with strongly correlated electrons, and quantum simulations of vibronic spectra^{124–127}, wavepacket evolution through conical intersections^{128–133} and algorithms for reduced dimensional reactive scattering studies^{134,135} do not appropriately describe quantum nuclear effects within hydrogen-bonded systems emanating from anharmonic effects and mode-coupling effects^{1–3,50,52,79,136}. Steps in the direction of developing a quantum algorithm for simulating explicit quantum wave packet dynamics on anharmonic electronic structure-based potential energy surfaces were taken in Refs. 137–139. In Ref. 137, a Hamiltonian mapping protocol was introduced to simulate the quantum nuclear dynamics in proton transfer reactions on spin-lattice quantum simulators. This was successfully implemented on Sandia National Labs’ Quantum Scientific Computing Open User Testbed (QSCOUT) ion-trap system as reported in Ref. 138 to study the vibrational spectra of the transferring proton in a short-strong hydrogen bonded system. A generalization of this scheme to higher nuclear dimensions using a tensor-network based formalism has recently been introduced in Ref. 139,140. A method to perform a parallel quantum computation of quantum wavepacket dynamics on a distributed set of ion-trap systems, along with implementation on IonQ’s 11-qubit Harmony ion-trap quantum systems is discussed in Ref. 139.

Quantum algorithms for simulating processes on quantum simulators can be broadly divided into two major classes: Hamiltonian or analog quantum simulation and unitary or quantum circuit decomposition (digital). In this paper, we discuss both—an analog Hamiltonian-based and a quantum circuit decomposition-based algorithm—to study spectroscopic features arising from anharmonic vibrations in small water clusters using quantum wavepacket dynamics. Hamiltonian or analog quantum simulation proceeds by mapping a desired Hamiltonian onto the quantum device’s Hamiltonian. This is done by programming the control parameters of the quantum device Hamiltonian. The mapping protocol in Ref. 137 simulates a chemical dynamics Hamiltonian on an ion-trap quantum computer by computing the control parameters of an Ising Hamiltonian, which describes the dynamics of ions in an ion-lattice. As a result, the ion-lattice dynamics directly correspond to the dynamics of the chemical system. The mapping protocol, however, is inherently approximate and only works well for systems with specific symmetries for a small number of qubits; errors grow with increasing number of qubits in this algorithm. Quantum circuit decomposition is more commonly used to write the unitary time-evolution operator corresponding to the Hamiltonian of a system in terms of

universal quantum gate sets. The circuit model, in theory, can be extended to an arbitrary number of qubits but suffers from increased circuit depth and exponentially increasing number of entangling gates as we scale up to a higher number of qubits. This results in increased measurement errors and loss of contrast in the measured probabilities due to the low fidelities of the entangling gates. For a more accurate implementation of quantum nuclear dynamics problems, we discuss a quantum circuit model-based approach to studying wavepacket dynamics. This decomposition technique is based on Quantum Shannon Decomposition (QSD)¹⁴¹.

The paper is organized as follows: In Section II, we discuss the Hamiltonian mapping protocol that was developed in Ref. 137. This approach is exact for three qubits, but becomes inherently approximate as the number of qubits grow. Hence, in Section III, we outline the Quantum Shannon circuit decomposition technique that is used to decompose the unitary propagator corresponding to the nuclear Hamiltonian. The algorithm presented in Section III yields a quantum circuit with the number of entanglement gates close to the theoretical lower bound¹⁴¹ and works for an arbitrary number of qubits. Both techniques use the first quantized form of the nuclear Hamiltonian computed in a grid representation. Numerical results are presented for both algorithms in Section IV B and IV C for the anharmonic molecular vibrations of the shared proton in short-strong hydrogen bonds^{27,142–144} that are present in protonated and hydroxide-rich water clusters. These include explicit numerical propagation of both the molecular dynamics problem, the mapped spin-lattice dynamics governed by Ising-type Hamiltonian as obtained from the mapping protocol, and quantum circuit decomposition using QSD. The Quantum Shannon Decomposition approach is implemented on Qiskit, and results from quantum simulation on a classical computer are provided here. The systems considered in Section IV are the H_5O_2^+ and H_3O_2^- ions. These low-barrier, short-strong hydrogen bonded systems^{7–9,144–147} are of fundamental significance in proton-transfer processes, and have a critical role in the enhanced mobility of protons and deuterons in condensed phase, in biological ion-channels and enzymes, and in fuel cells^{148–151}. We inspect the vibrational properties of these systems using quantum algorithms presented here. Conclusions are given in Section V.

II. QUANTUM ALGORITHMS FOR WAVEPACKET DYNAMICS: MAPPING PROTOCOLS FOR SPIN-LATTICE SIMULATIONS

The generalized form of the Ising Hamiltonian can be used to describe the interactions of spin-states on a spin lattice. The mapping protocol introduced in Ref. 137 relates a quantum nuclear Hamiltonian, involving the nuclear kinetic energy and the Born-Oppenheimer po-

tential surface obtained from electronic structure theory, to a generalized Ising Hamiltonian realizable on a range of quantum systems including ion trap quantum simulators. The inherent symmetries of the Ising Hamiltonian which describes the dynamics of effective spin-states on a lattice and that of the Born-Oppenheimer potential and nuclear kinetic energy are exploited to arrive at the map. In the following sections, we provide the transformations and their geometric interpretations that expose these symmetries in the Ising (Section II A) and the nuclear Hamiltonian (Section II B). The parameters of the Ising Hamiltonian that are programmable on a lattice of ions are computed from the quantum nuclear Hamiltonian and the algorithm is summarized in Section II C. For details, the reader is directed to Ref 137.

A. The role of geometric structure in generalized Ising Hamiltonians towards achieving a map to quantum nuclear dynamics

Any two-level quantum system can be mapped to a spin-1/2 particle in an effective magnetic field. In the ion trap used in Ref. 138, the qubit levels encoded onto the $^2S_{1/2}$ state, namely, $|F=0, m_F=0\rangle$ and $|F=1, m_F=0\rangle$ hyperfine ‘clock’ states of $^{171}\text{Yb}^+$ ions are mapped onto the two levels of a spin-1/2 particle and denoted as $|0\rangle$ and $|1\rangle$, respectively¹⁵². In its most generalized form, the Ising Hamiltonian that can be implemented on the ion-trap is given by,

$$\mathcal{H}_{IT} = \sum_{i=1}^{N-1} \sum_{j>i}^N \{J_{ij}^x \sigma_i^x \sigma_j^x + J_{ij}^y \sigma_i^y \sigma_j^y + J_{ij}^z \sigma_i^z \sigma_j^z\} + \sum_{i=1}^N \{B_i^x \sigma_i^x + B_i^y \sigma_i^y + B_i^z \sigma_i^z\} \quad (1)$$

where $\{\sigma_i^x, \sigma_i^y, \sigma_i^z\}$ are the Pauli spin operators on the i -th lattice site along the respective spatial direction. The energy gap between the states at each ion, i , and their relative orientations are controlled by local effective magnetic fields, $\{B_i^x, B_i^y, B_i^z\}$, and the spin-spin coupling between different lattice sites, i and j , is controlled using laser pulses, also spatially non-isotropic, and represented as $\{J_{ij}^x, J_{ij}^y, J_{ij}^z\}$. It is critical to note that the expression above is more general than the form of the Ising Hamiltonian commonly used in condensed matter physics^{153–155}, NMR, other zero-field splitting studies¹⁵⁶ where only nearest-neighbor interactions or spin-lattice sites within a certain spatial distance may interact and magnetic fields only across certain directions are considered, and transverse Ising models^{157–159} implemented for adiabatic quantum computing for electronic structure studies¹⁶⁰. The magnetic fields and inter-site coupling parameters, $\{J_{ij}^\gamma, B_i^\gamma\}$ with $\gamma \in \{x, y, z\}$, form a set of programmable parameters that can be manipulated to simulate a general form of the Ising-type Hamiltonian,

as in Eq. (1), on a lattice of ions.

The Ising Hamiltonian structure exhibits inherent symmetries in terms of these control parameters, that can be exploited to map a class of Hamiltonians to the quantum simulator. In Ref. 137, we show how a certain permutation of the computational basis in which such Hamiltonians are conventionally represented, reveals a block structure of the Hamiltonian. Here, we provide a geometric visualization of the computational basis set ordering scheme through a generalized representation of the Bloch sphere. Through this geometric representation, we illustrate the classification of the computational basis that exposes the inherent symmetries in the Ising Hamiltonian. Consequently, we discuss and illustrate the structure of the Ising Hamiltonian in this ordered basis set.

Conventionally, the spin-lattice Hamiltonian is represented in the 2^N -dimensional space of spin- $\frac{1}{2}$ states where each spin state corresponds to a two-level system that can either be up or down and equivalently $|0\rangle$ or $|1\rangle$. A Bloch sphere (Figure 1(a)) provides a geometrical representation of all pure states of a single spin system. To generalize the Bloch sphere representation for a single spin to a higher number of spins, we borrow the idea of q-sphere from IBM Qiskit¹⁶¹, to geometrically represent all 2^N spin states of an N -qubit system. Figure 1 complements our discussion.

The q-sphere for an N -qubit system ($N \geq 2$) is divided into rungs as follows. We begin by placing the all-down state $|00 \dots 0\rangle$ at the bottom pole or the 0^{th} rung of the q-sphere. We then apply the total spin raising operator on this state, one spin at a time to obtain all other states in the higher rungs of the sphere. The action of the total spin raising operator once on the 0^{th} rung yields all N -states that correspond to a single spin up and $N-1$ spins down. These are represented on a single plane close to the $|00 \dots 0\rangle$. See Figure 1. The action of the total spin-raising operator on all states of this rung yields all possible $N(N-1)/2$ states of the 2^{nd} rung, and these states are represented on the next plane. As we go to higher qubits, all possible ${}^N C_n$ states for the n^{th} rung are obtained. This way, all basis states in the spin-lattice system are represented on the q-sphere and the number of states in each rung of the q-sphere are identical to those encountered in Pascal’s triangle. All combinations of spin states with the same total S_z -value occupy the same rung.

The geometrical representation of the N -qubit basis states using the q-sphere representation lends itself naturally to the classification of basis states we discuss for representing the Ising Hamiltonian. In Ref.137, we note that the basis vectors created from acting an even number of lattice-site spin raising operators, $\{S_i^+\}$ on the full downspin state, $|00 \dots 0\rangle$, yield the set, $\{|00 \dots 0\rangle; S_i^+ S_j^+ |00 \dots 0\rangle; S_i^+ S_j^+ S_k^+ S_l^+ |00 \dots 0\rangle; \dots\}$, that are grouped as part of one block of the ion-trap Hamiltonian and those that are obtained using an odd number of raising operators: $\{S_i^+ |00 \dots 0\rangle; S_i^+ S_j^+ S_k^+ |00 \dots 0\rangle; \dots\}$

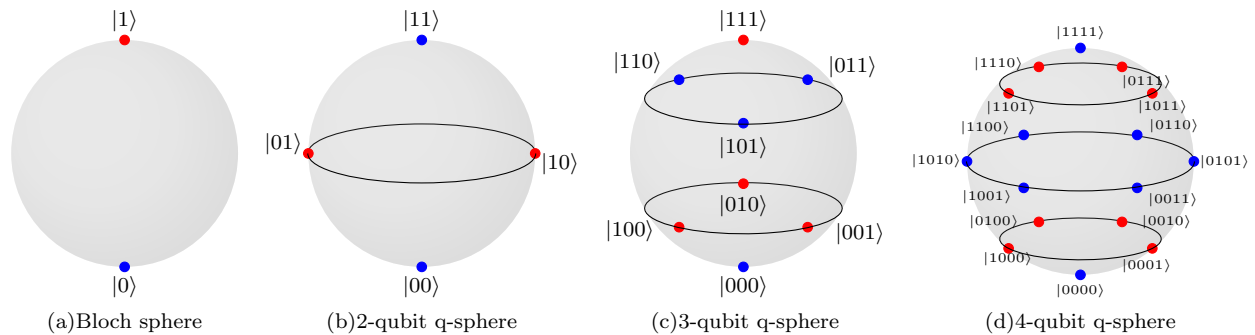


FIG. 1: A generalized Bloch sphere for an arbitrary number of qubits, along with the classification of basis states shown using red and blue colors.

are grouped into a second block. The states belonging to the same block are represented using the same color (blue or red) in Figure 1. As can be seen in the q-sphere representation in Figure 1, the action of the odd and even number of site-specific spin-raising operators on the all down spin state $|00\dots 00\rangle$ correspond to its alternating rungs. The alternating rungs can now be grouped to form the two basis set blocks in which the Ising Hamiltonian has a block structure as discussed below and shown in Figure 2.

The diagonal elements of the Ising Hamiltonian, when represented in the computational basis, are linear combinations of all $\{J_{ij}^z, B_i^z\}$ parameters. Figure 2 does not show these to maintain clarity. Since, inside each block of the permuted computational basis, the bases differ by at least two spin flips, the bases inside each block are connected by spin-spin coupling parameters $\{J_{ij}^x, J_{ij}^y\}$ (shown in shades of purple in Figures 2a-c). Between the two blocks, the pairs of bases that differ by a single spin flip or an odd number of flips are coupled by the $\{B_i^x, B_i^y\}$ parameters and hence those form the elements of the off-diagonal blocks of the Ising Hamiltonian in this permuted basis (as shown in green shades in 2a-c). The structure derived here is completely general for N qubits as can be seen in Figures 2 (a), (b), and (c) for two, three, and four qubits, respectively.

Furthermore, the diagonal and off-diagonal blocks for the N -qubit Ising Hamiltonian can be recursively obtained from those of the $N - 1$ qubit Hamiltonian. This recursive structure within each block of the Ising Hamiltonian is illustrated in Figures 2 (a), (b), and (c) using a gradient in colors, purple for the diagonal blocks with $J_{ij}^x \pm J_{ij}^y$ elements and green for the off-diagonal blocks with $B_i^x \pm iB_i^y$ matrix elements. For example, the recursion can be seen as follows for the diagonal block containing elements with spin-spin interaction terms. We begin with the elements of the diagonal block for a 2-qubit Ising Hamiltonian as in Figure 2 (a), $J_{ij}^x \pm J_{ij}^y$ for $i = 1$, and $j = 2$ corresponding to the only spin-spin interaction in a two-qubit system shaded the darkest in all Figures 2 (a), (b), and (c). The introduction of a third qubit introduces all possible spin-spin interactions

$J_{i3}^x \pm J_{i3}^y$ for all $i \leq 2$ as shown with the next shade of purple in Figure 2 (b). Similarly, all possible spin-spin interactions $J_{i4}^x \pm J_{i4}^y$ for $i \leq 3$ also appear in the diagonal blocks of the 4-qubit Ising Hamiltonian as shown using the lightest shade of purple in Figure 2 (c). The 2- and 3-qubit diagonal block elements are nested in the 4-qubit Ising Hamiltonian. Therefore, with each additional qubit, the structure of the $N - 1$ qubit Ising Hamiltonian is preserved, and blocks containing $J_{iN}^x \pm J_{iN}^y$ for all $i \leq N - 1$, the interaction of the N^{th} spin with the $N - 1$ spins are added. The off-diagonal blocks also have a similar recursive structure, wherein with the addition of a qubit, a block with elements $B_N^x \pm iB_N^y$ is added to the Ising Hamiltonian. This is made clear in Figures 2 (a)-(c) with the gradation in green used for $B_1^x \pm iB_1^y$, $B_2^x \pm iB_2^y$, and $B_N^x \pm iB_N^y$ elements in the Hamiltonians. This block-form of the Ising-type Hamiltonian and the associated structure in Figure 2, is a significant general result¹³⁷. To the best of our knowledge, such a structure of the general Ising model was first discussed in Ref 137, and we see that this analysis is critical for mapping arbitrary problems.

B. Nuclear Hamiltonian: Transformations that yield a block diagonal structure

The nuclear Hamiltonian is computed using a coordinate representation, where the dimension along the donor-acceptor axis is discretized into 2^N points. The matrix elements of the nuclear Hamiltonian, \mathcal{H}_{Mol} in this coordinate representation, $\{|x_i\rangle\}$ is therefore given by

$$\langle x | \mathcal{H}_{Mol} | x' \rangle = K(x, x') + V(x)\delta(x - x') \quad (2)$$

The potential energy for the quantum dimensions is computed using standard electronic structure methods for which further details for each system are provided in the results section. The nuclear kinetic energy in this grid representation is approximated using the analytic banded Toeplitz Distributed Approximating Functionals

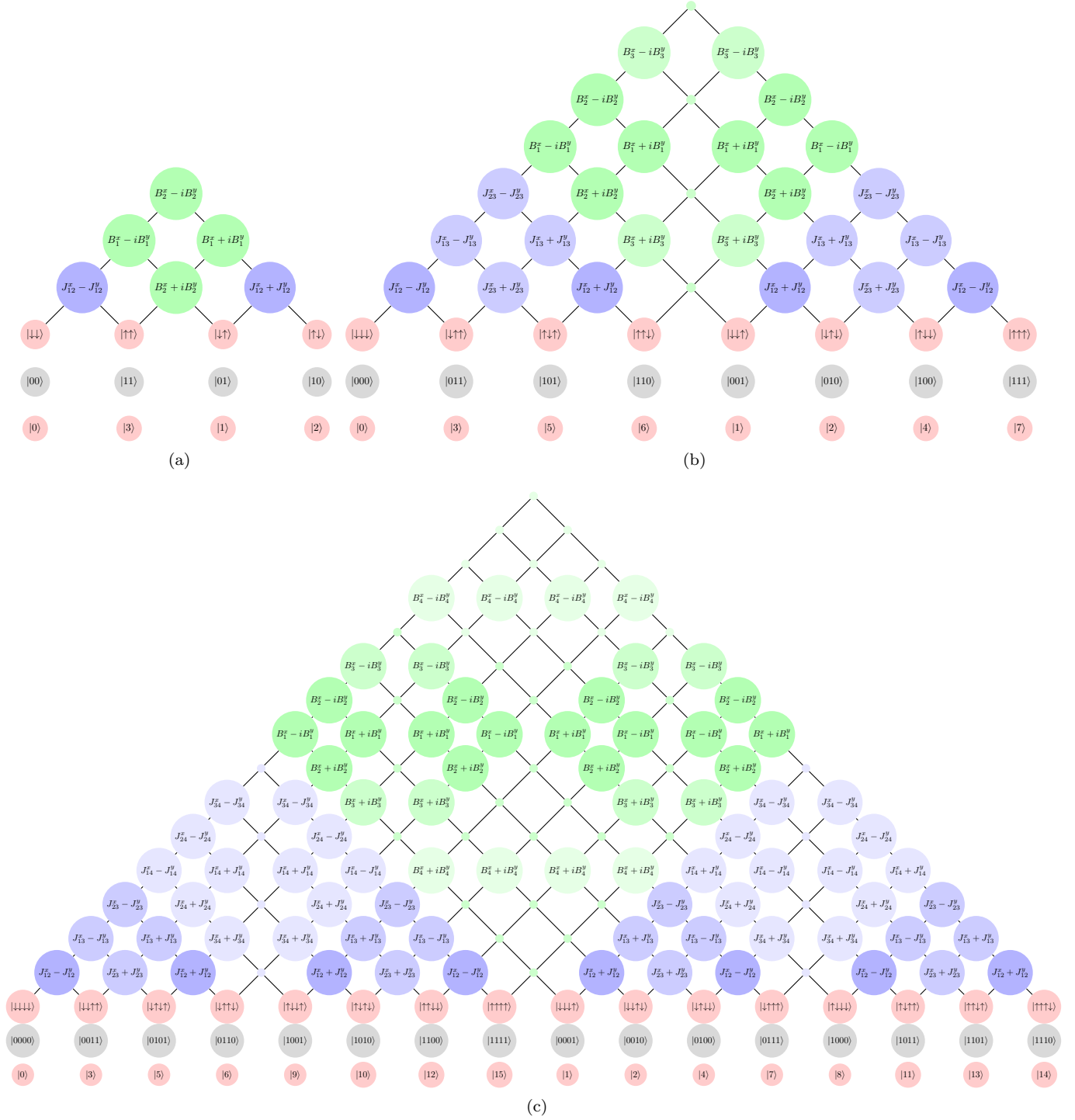


FIG. 2: Recursive block structure of the Ising Hamiltonian in Eq. (1) for three (a) and four (b) qubits. The upper triangular portion of the Hamiltonian matrix is shown (excluding the diagonal). The computational basis is partitioned into odd, $\{\mathbf{S}^{+2n-1} |00\dots\rangle\}$, and even, $\{\mathbf{S}^{+2n} |00\dots\rangle\}$, spans of the total spin raising operators. The interaction between states, $|i\rangle$ and $|j\rangle$ is the ij^{th} matrix element of the ion trap Hamiltonian. For example in (b), $\langle 0101 | \mathcal{H}_{\mathcal{IT}} | 1111 \rangle = J_{13}^x - J_{13}^y$. The off-diagonal block that couples the odd and even spans of the total spin-raising operators are marked in green. Zero coupling is represented with a “dot”.

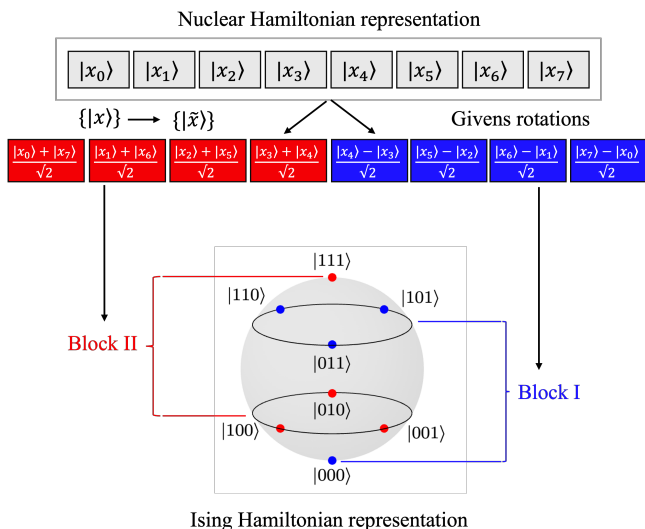


FIG. 3: The classification of the Givens-transformed grid bases, and the permuted computational bases in the q-sphere representation. Note that the Givens rotations result in symmetric and anti-symmetric combinations of pairs of symmetrically located grid basis states. The map between the transformed Hamiltonians results from a map between the corresponding blocks of the basis of representation.

(DAFs)^{162,163}.

$$K(x, x') = K(|x - x'|) = \frac{-\hbar^2}{4m\sigma^3\sqrt{2\pi}} \exp\left\{-\frac{(x - x')^2}{2\sigma^2}\right\} \sum_{n=0}^{M_{DAF}/2} \left(\frac{-1}{4}\right)^n \frac{1}{n!} H_{2n+2} \left(\frac{x - x'}{\sqrt{2}\sigma}\right). \quad (3)$$

where, $H_{2n+2} \left(\frac{x-x'}{\sqrt{2}\sigma}\right)$ are the even order Hermite polynomials that only depend on the spread separating the grid basis vectors, $|x\rangle$ and $|x'\rangle$, and M_{DAF} and σ are parameters that together determine the accuracy and efficiency of the resultant approximate kinetic energy operator. The nuclear Hamiltonian, \mathcal{H}_{Mol} in this coordinate representation, $\{|x_i\rangle\}$, therefore has a banded Toeplitz structure due to the structure of the kinetic energy when expressed in terms of DAFs. This banded-Toeplitz representation of the DAF approximation for the kinetic energy operator in eq. 3, where the property of its matrix elements, $K_{ij} \equiv K(|i - j|)$, has a critical role in reducing the nuclear Hamiltonian to the form of \mathcal{H}_{IT} as discussed in Ref. 137 and summarized in Section II C.

The Householder and Givens transformations are commonly used matrix transformations that allow arbitrary matrices to be reduced to canonical forms¹⁶⁴. Here, we use a sequence of Givens transformations to transform the banded Toeplitz form of the nuclear kinetic energy operator into a block diagonal form, $\tilde{\mathcal{H}}_{Mol}$ that is com-

mensurate with that of the Ising Hamiltonian in the permuted spin basis, as discussed in Section II. The details of the exact transformation are presented in section A of the SI. Furthermore, this block diagonal form is maintained, when the one-dimensional potential energy surface belongs to the C_s point group, whose only symmetry operations are identity and reflection about a mirror plane. For cases where such symmetry does not exist, the more general set of transformations shown in Section III may be employed. The Givens matrix elements are the characters of this point group and thus with each Givens transformation, a rotation is effected in the two-dimensional plane of the pair of symmetrically located grid basis states. The resulting Givens transformed basis, $\{|\tilde{x}_i\rangle\}$ from the corresponding grid basis, $\{|x_i\rangle\}$ is illustrated in Figure 3 for the case of eight grid points. We, therefore, exploit the banded Toeplitz symmetry of the DAF kinetic energy operator and symmetry of the potential energy surface. The details of this transformation can be found in SI section A and Ref. 137, where the explicit transformations of each matrix element of the transformed Hamiltonian are given in terms of the elements of the banded Toeplitz Hamiltonian and the elements of the Givens matrices.

C. Obtaining ion-trap parameters, $\{B_i^z, J_{ij}^z\}$ from transformed nuclear Hamiltonian

As seen from the discussions in Sections II A and II B, the Ising Hamiltonian and the nuclear Hamiltonian both have block structures resulting from the permutation of the computational basis and the Givens transformation of the grid basis, respectively. Owing to their commensurate structures, a direct map between each element of the nuclear Hamiltonian, \mathcal{H}_{Mol} in the $\{|\tilde{x}_i\rangle\}$ basis to the corresponding elements of the Ising Hamiltonian, \mathcal{H}_{IT} can be generated to compute the Ising Hamiltonian parameters. Our goal is to use the diagonal and off-diagonal elements of $\tilde{\mathcal{H}}_{Mol}$ to obtain the sets of ion-trap parameters $\{B_i^z, J_{ij}^z\}$ and $\{J_{ij}^x, J_{ij}^y\}$, respectively. This establishes a map between the givens transformed grid basis and the permuted computational basis, as is shown in Figure 3. The mapping expression between the elements of the molecular Hamiltonian and the corresponding elements of the ion-trap Hamiltonian may be written as

$$\langle \tilde{x} | \mathcal{H}_{Mol} | \tilde{x}' \rangle \equiv \langle \tilde{\lambda} | \mathcal{H}_{IT} | \tilde{\lambda}' \rangle \quad (4)$$

for $|\tilde{\lambda}\rangle$ corresponding to the computational bases in blocks I or II for the Ising Hamiltonian (as discussed in Section II A and shown in Figures 1 and 3). Using Eq. (2) and the transformations discussed in Section II B (detailed in SI A) to write the elements of $\tilde{\mathcal{H}}_{Mol}$ and the corresponding Ising Hamiltonian matrix elements for Eq. (1), for the left and right sides of Eq. (4) corresponding

to the diagonal elements only, we obtain

$$\begin{aligned} & [K(x_i, x_i) - K(x_i, x_{n-i})] + \frac{1}{2} [V(x_i) + V(x_{n-i})] \\ &= \sum_{j=1}^N (-1)^{\tilde{\lambda}_j} B_j^z + \sum_{j=1}^{N-1} \sum_{k>j}^N (-1)^{\tilde{\lambda}_j \oplus \tilde{\lambda}_k} J_{jk}^z \\ & \hspace{15em} \text{for } i \leq n/2 \end{aligned} \quad (5)$$

$$\begin{aligned} & [K(x_i, x_i) + K(x_i, x_{n-i})] + \frac{1}{2} [V(x_i) + V(x_{n-i})] \\ &= \sum_{j=1}^N (-1)^{\tilde{\lambda}_j} B_j^z + \sum_{j=1}^{N-1} \sum_{k>j}^N (-1)^{\tilde{\lambda}_j \oplus \tilde{\lambda}_k} J_{jk}^z \\ & \hspace{15em} \text{for } i > n/2 \end{aligned} \quad (6)$$

where \oplus on the right side denotes the addition modulo 2, $\tilde{\lambda}_j$ is the j^{th} bit of the bit representation of $|\tilde{\lambda}\rangle$ with values 0 or 1 as shown in Figures 1 and 2.

A detailed discussion on this map is provided in Ref. 137 where it is shown that the ion-trap control parameters, $\{B_i^z; J_{ij}^z\}$ are specific Hadamard transforms of $\langle \tilde{x} | \mathcal{H}_{Mol} | \tilde{x} \rangle$. In a similar manner, the off-diagonal elements of \mathcal{H}_{Mol} are mapped to the corresponding \mathcal{H}_{IT} elements to obtain the $\{J_{ij}^x; J_{ij}^y\}$ parameters. The map is approximate for a higher number of qubits, for which the error estimates are provided in Ref. 137. In Figure 4, the map is illustrated for the H_3O_2^- system to be studied later in the publication.

The reasons behind the intrinsically approximate nature of the mapping algorithm are discussed in detail in Ref. 137. We summarize the main features here. In essence, as the number of qubits N increases, the Ising Hamiltonian parameters (B and J handles in Eq. (1)) scale as,

$$\{N + N(N-1)/2\} + \{N(N-1)\} \rightarrow \mathcal{O}(N^2), \quad (7)$$

Here (a) the first quantity, $\{N + N(N-1)/2\}$, refers to the parameters, $\{B_i^z; J_{ij}^z\}$, that form the diagonal elements of the Ising matrix, (b) the second quantity on the left, $\{N(N-1)\}$, refers to the parameters, $\{J_{ij}^x \pm J_{ij}^y\}$, that control the off-diagonal elements. This scaling and structure of the spin-lattice Hamiltonian¹³⁷, may restrict the mapping of a general unitary operator, since a general $2^N \times 2^N$ unitary matrix may have $\mathcal{O}(2^N)$ independent elements. Thus, as the number of qubits increases, the mapping algorithm becomes more and more approximate as the number of equations given by Eqs. (5) and (6) exceeds the number of spin-lattice parameters $\{B_i^z; J_{ij}^z\}$. However, it may also be possible to reduce the number of actual parameters within the $2^N \times 2^N$ unitary matrix and these aspects will be considered in future publications¹³⁹.

III. QUANTUM SHANNON DECOMPOSITION: REDUCTION OF ARBITRARY UNITARY OPERATIONS INTO QUANTUM CIRCUITS

The mapping protocol necessitates that the number of $\{B_i^x, B_i^y, B_i^z\}$, and $\{J_{ij}^x, J_{ij}^y, J_{ij}^z\}$ parameters in the Ising Hamiltonian match the number of parameters in the molecular Hamiltonian. Since we also consider a fine grid for our potential energy surface with an equivalent increase in the number of qubits, it is critical to note that the molecular Hamiltonian matrix size grows exponentially while the number of Ising Hamiltonian parameters only grows quadratically (See Ref. 137). Consequently, the map between the molecular Born-Oppenheimer Hamiltonian and the Ising Hamiltonian becomes more and more approximate as the number of qubits grows. To address this and achieve accurate treatment of the chemical dynamics process for a larger number of qubits, we introduce a quantum circuit decomposition method here. The unitary propagator corresponding to the molecular Hamiltonian is written as a quantum circuit which is then used to simulate the temporal evolution of the molecular system. It has been shown that an arbitrary unitary matrix can be decomposed into a universal quantum gate set consisting of a few single qubit gates along with a two-qubit entangling gate¹⁶⁵. Several matrix decomposition techniques such as the QR, Givens, Householder, and cosine-sine decomposition have been used to obtain quantum circuits for arbitrary unitary operators^{165,166} resulting in universal quantum gate sets. In this section, we adapt the Quantum-Shannon decomposition¹⁴¹(QSD) for the quantum circuit decomposition of unitary matrices obtained in quantum chemical dynamics processes. The decomposed unitaries are the equivalent to unitary gate operations that can be implemented using standard quantum gates from a universal gate set on quantum hardware. This allows executing an arbitrary unitary operation as a concatenated sequence of universal gates on a given quantum hardware. The decomposition scheme involves two well-known matrix decomposition schemes - the cosine-sine decomposition (CSD)¹⁶⁷⁻¹⁶⁹ and the joint eigenvalue-based decomposition of block diagonal unitaries referred to here as VDW¹⁶⁶ scheme. A brief description of the algorithm is provided below. One key outcome from the algorithm below is that the number of entangling gates in this algorithm can be estimated at $\frac{3}{4}4^n - \frac{3}{2}2^n$ which is close to the theoretical lower bounds to the number of CNOT gates, $\frac{1}{4}(4^n - 3n - 1)$, as discussed in Ref. 141.

We begin by considering a 2^N by 2^N unitary matrix that is to be implemented on a quantum computer using universal gates. We consider the universal gate set $\{R_y(\theta), R_z(\theta), \text{CNOT}\}$, consisting of single qubit rotation operations, $R_y(\theta)$ and $R_z(\theta)$ that affect rotations about the y and z axis of the Bloch sphere by arbitrary angles θ , and the two-qubit operation, CNOT. A flow of the decomposition is provided as a tree diagram in Figure 5. The CSD (shown in red in Figure 5) and VDW

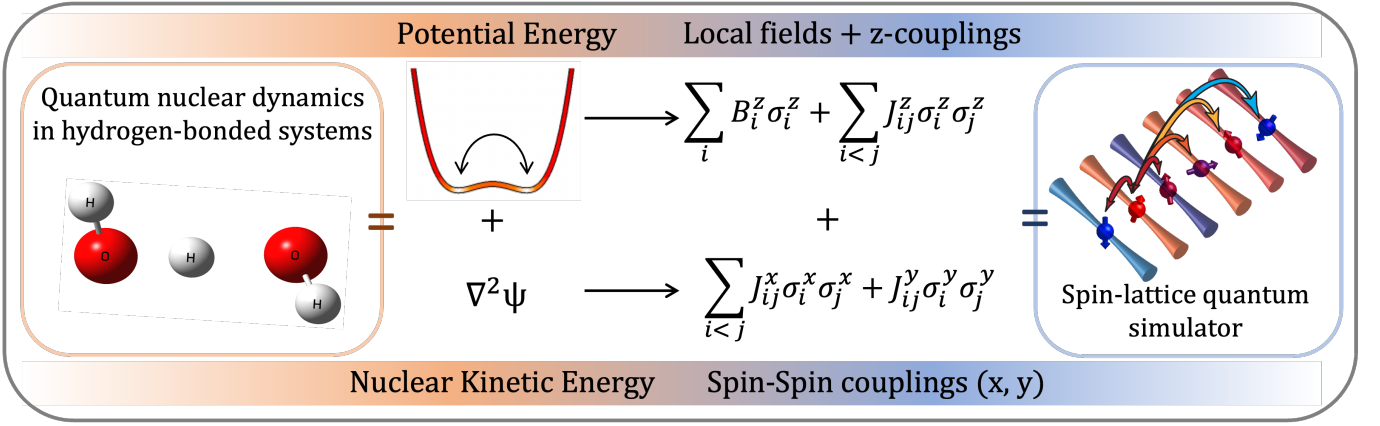


FIG. 4: An outline of the mapping algorithm: The algorithm converts the Born-Oppenheimer potential surface and kinetic energy terms in a quantum-nuclear problem to a set of controllable ion-trap parameters, $\{\{B_i^z\}; \{J_{ij}^x, J_{ij}^y, J_{ij}^z\}\}$, and facilitates the dynamical evolution of quantum states in an ion trap.

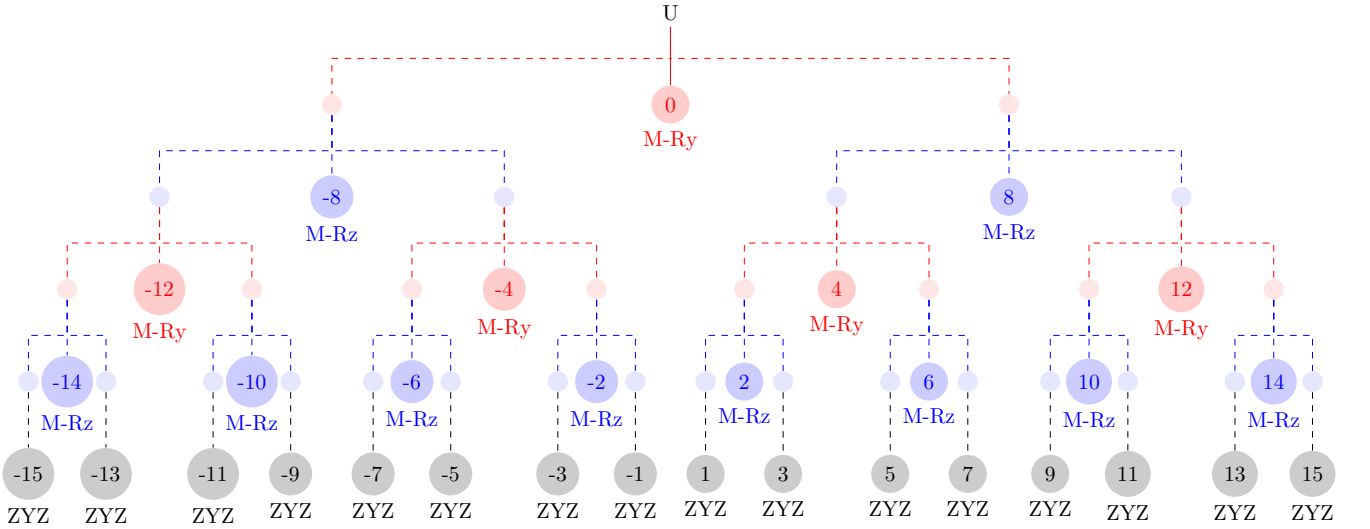


FIG. 5: Decomposition of a 3-qubit unitary, U , into one and two-qubit gates. The decomposition involves alternate layers of CSD (red) and VDW (blue). M-Rz(Ry) are N and $N - 1$ qubit multiplexed Rz(Ry) gates which can be further decomposed into a set of CNOT and Rz(Ry) gates. The ultimate layer (gray) involves the decomposition into single qubit gates.

(shown in blue in Figure 5) steps iteratively break down the 2^N by 2^N unitary to a sequence of these single and two-qubit operations. The CSD decomposes the unitary matrix, U , into a product of three unitaries with distinct structures,

$$U = \begin{pmatrix} \mathbf{L}_0 & \mathbf{0} \\ \mathbf{0} & \mathbf{L}_1 \end{pmatrix} \begin{pmatrix} \mathbf{C} & -\mathbf{S} \\ \mathbf{S} & \mathbf{C} \end{pmatrix} \begin{pmatrix} \mathbf{R}_0 & \mathbf{0} \\ \mathbf{0} & \mathbf{R}_1 \end{pmatrix} \quad (8)$$

where the left(L) and right(R) matrices are block diagonal unitaries with blocks \mathbf{L}_0 , \mathbf{L}_1 and \mathbf{R}_0 , \mathbf{R}_1 , respectively. \mathbf{C} and \mathbf{S} are diagonal matrices with entries $\cos(\alpha_i)$ and $\sin(\alpha_i)$, respectively for $i = 0 - 2^{N-1}$. This cosine-sine (CS) matrix (node 0 in Figure 5) is a multiple-control R_y gate. A multi-control¹⁴¹ gate can be cast as

an N -qubit generalization of a conditional gate in a quantum circuit, wherein each of the 2^{N-1} conditions implemented using $N - 1$ control qubits results in a different unitary operation on the N^{th} target qubit. These may be thought of as $CCC \cdots R_y$ operations. A multi-control R_y can, therefore, be thought of as a conditional operation of a $R_y(\alpha_i)$ rotation on the target qubit depending on the i^{th} condition enforced by $N - 1$ qubits. This simultaneous operation of the 2^{N-1} $R_y(\alpha_i)$'s for all values in $\{\alpha_i\}$ can be decomposed further and implemented using 2^{N-1} CNOT's and 2^{N-1} $R_y(\theta_i)$ rotation gates. The rotation angles θ_i can be obtained from linear combinations of α_i 's using a Gray code method as outlined in Ref. 170. Classically, one can think about this as 2^{N-1} conditionality statements, one condition representing a specific R_y

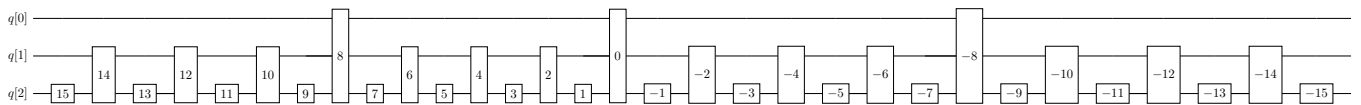


FIG. 6: Schematic of the circuit resulting from the Quantum Shannon decomposition for an arbitrary three-qubit unitary matrix. All single qubit operations (on $q[2]$) are decomposed using the ZYZ decomposition, while all multi-qubit operations are either multi-controlled R_y or R_z operations as discussed in Section III and Figure 5.

rotation, only, on a quantum computer these are meant to be executed in parallel. While such operations may in principle represent the true power of quantum devices in the future, in the NISQ era^{171,172}, these operations are deeply limited by the number of CNOT gates required to implement them.

The block diagonal unitaries on the left and right in Eq. (8) (red empty nodes in Figure 5), are N -qubit conditional gates, known as quantum multiplexors, with a single qubit control and corresponding conditional operation on $N - 1$ target qubits. At this point, it is important to reiterate and note the difference in the structures of the block diagonal L , R matrices and the CS matrix and the resulting multi-qubit gates. While the N -qubit operation corresponding to the CS unitary matrix, as discussed earlier, has multiple controls (precisely 2^{N-1} for an N qubit unitary), and a single target qubit, that for the L , R matrices have a single control with $N - 1$ target qubits. This decomposition technique thus exploits these two generalizations to multi-qubit gates to build the entire quantum circuit corresponding to U . The VDW transformation, as given by eq. 9, is a technique for decomposing such quantum multiplexor gates (obtained from the L and R matrices above), with a single control and multiple target qubits, into basic quantum circuit unitaries. The L and R matrices from Eq. (8) are thus further decomposed into,

$$L = \begin{pmatrix} \mathbf{L}_0 & \mathbf{0} \\ \mathbf{0} & \mathbf{L}_1 \end{pmatrix} = \begin{pmatrix} \mathbf{V} & \mathbf{0} \\ \mathbf{0} & \mathbf{V} \end{pmatrix} \begin{pmatrix} \mathbf{D} & \mathbf{0} \\ \mathbf{0} & \mathbf{D}^\dagger \end{pmatrix} \begin{pmatrix} \mathbf{W} & \mathbf{0} \\ \mathbf{0} & \mathbf{W} \end{pmatrix} \quad (9)$$

The VDW is critical in that left and right block diagonal matrices containing \mathbf{V} and \mathbf{W} , respectively correspond to $N - 1$ qubit operations in a quantum circuit. Therefore, each VDW step in the decomposition halves the dimension of the unitary matrix. This step is shown in blue in Figure 5 and the \mathbf{V} and \mathbf{W} matrices are blue nodes in Figure 5). The \mathbf{V} and \mathbf{W} matrices are further decomposed using CSD in the next step. The diagonal matrix, \mathbf{D} , (node -8 for L and 8 for R in Figure 5) is a multi-control R_z gate (similar to the multi-control R_y operation for the CS matrix) and can be decomposed further into a sequence of 2^{N-1} CNOT's and 2^{N-1} $R_z(\theta)$ gates, similar to the decomposition of the cosine-sine matrix as a multiplexed $R_y(\theta)$. As noted above, these multiplexed $R_z(\theta)$ operations are also akin, now, to 2^{N-2} conditional statements. Following $N - 1$ steps of alternating CSD and VDW steps, the resultant matrices are single-qubit unitaries, which are further decomposed using the ZYZ

scheme for arbitrary single-qubit unitaries. The multiplexors are decomposed into single qubit rotation gates and CNOT gates using a gray code implementation as outlined in Ref. 170. Thus, the QSD yields a quantum circuit of multi-controlled $R_y(\theta)$ and $R_z(\theta)$ gates, and single qubit unitaries, which have standard procedures to be further decomposed into the gates in the universal gate set $\{R_y, R_z, CNOT\}$. The numbered nodes of Figure 5 correspond to these multi-controlled and single qubit unitaries and for clarity, the circuit schematic corresponding to the decomposition is provided in Figure 6. Note the order is reversed in the quantum circuit for showing the action of U on an initial qubit state.

The number of gates in any standard implementation of this decomposition is estimated from the implementation of the multi-controlled $R_y(\theta)$ and $R_z(\theta)$ gates. This scheme has the advantage that when a fixed gate set is used to construct the circuit, the resulting circuits have a constant circuit depth for an arbitrary 2^N by 2^N dimensional unitary. This implementation assumes the use of the universal gate set $\{R_y, R_z, CNOT\}$ as is apparent from the summary above, but is not limited by this gate set alone. Each 2^N by 2^N multiplexed-Ry(Rz) requires 2^{N-1} CNOTs and 2^{N-1} Ry(Rz) gates using the gray code implementation as discussed in 141. There is an inherent structure in the decomposition scheme that is evident from the decomposition of general multiplexed R_y and R_z gates as shown in reference 141. This structure of the decomposition is irrespective of the inherent symmetries present in the unitary itself.

IV. PROTON STRETCH DYNAMICS IN H_5O_2^+ AND H_3O_2^- USING THE MAPPING PROTOCOL AND USING QUANTUM SHANNON DECOMPOSITION

We examine the map in Section II and the quantum circuit decomposition method in Section III by simulating and comparing the quantum dynamics of the shared proton in the protonated Zundel (H_5O_2^+) and the corresponding hydroxide water clusters (H_3O_2^-). In examining the mapping protocol, we simulate and compare the dynamics of both the molecular systems and their corresponding ion-trap dynamics, on classical hardware, independently. The Ising model Hamiltonian that we consider for validating the mapping protocol is for a trapped ion system with three qubits. In simulating the proton-transfer dynamics for each of the systems, we study the

time evolution of initial nuclear wavepacket states prepared in the respective permuted basis representations for the molecular and Ising model Hamiltonians. As stated, the parameters in the Ising Hamiltonian are determined, and thus controlled, by the pre-computed matrix elements of the molecular Hamiltonian. In implementing the circuit decomposition technique, we simulate the unitary time evolution of the transferring proton in the water clusters by decomposing the unitary propagator, $e^{-i\hat{H}t/\hbar}$, for each value of t into a sequence of quantum gates using the Quantum Shannon decomposition method detailed in Section III. We implement the resulting quantum circuits on IBM’s QASM simulator using their software development kit, Qiskit. In the following sections, we first introduce the molecular systems we consider to validate our mapping protocol and circuit decomposition scheme. In Section IV A, we outline the computational details of the potential energy surfaces and the quantum nuclear Hamiltonian, followed by the time evolution of the quantum nuclear wavepacket, for both the systems under consideration in Sections IV B and IV C.

Water clusters are an important class of molecular systems found in many constrained environments such as biological membranes, enzyme active sites,^{173,174} and ion channels¹⁷⁵. Water-mediated “proton wires,” for example, are routinely invoked to explain charge transport across cell membranes and the primary charge-separation step in photosynthesis. They may also be confined within carbon nanotubes leading close to ballistic transport,^{176–178} and are a critical aspect of polymer electrolyte fuel cells.¹⁷⁹ The lighter mass of the hydrogen nucleus makes quantum nuclear effects critical in all such cases;^{180–183} additionally the multidimensional quantum nuclear effects in such systems arising from the vibrational coupling between the proton-transfer dimensions and other orthogonal modes is also known to be critical in such problems.^{1,52,64,65}

The chemical systems considered in this publication are specific small protonated and hydroxide-rich water clusters. The isolated H_5O_2^+ and H_3O_2^- ions are two of the most fundamental structures involved in the proton-transfer process. The anionic H_3O_2^- complex is especially interesting because it involves a strong low-barrier hydrogen bond (LBHB),^{7–9,146,147} a phenomenon often introduced to explain the surprisingly high rates of some enzyme-catalyzed reactions^{143,144,184,185}. Based on the studies of small molecules, such short-strong HBs are often formed between functional groups with comparable pKa’s, and often result in a zero point energy for the shared hydrogen higher than the barrier height energy for proton transfer. The Zundel cation is a small prototypical system with a proton shared between two water molecules forming a short, strong hydrogen bond^{52,64,65,72,74,81,136}. This system plays a fundamental role in the understanding of processes such as the enhanced mobility of protons and deuterons in condensed phase aqueous environments, in biological sys-

tems, and several problems of interest in materials chemistry, such as protonic conductors and fuel cells^{148–151}. Due to their central role in aqueous charge transport, the H_5O_2^+ and H_3O_2^- ions have been extensively investigated with electronic structure theory and quantum nuclear dynamics^{64,72,81}, and both display stable configurations where one hydrogen atom resides between the two oxygen atoms (e.g., $[\text{H}_2\text{O}\cdots\text{H}\cdots\text{OH}_2]^+$ and $[\text{HO}\cdots\text{H}\cdots\text{OH}]^-$).

A. Computation of the nuclear Hamiltonians describing proton transfers in H_3O_2^- and Zundel clusters

We compute one-dimensional potential energy surfaces for the intra-molecular proton transfer mode in both H_3O_2^- and H_5O_2^+ , by first locating a stationary point for both systems where the proton is symmetrically shared between the donor and acceptor groups. For the case of H_3O_2^- , this corresponds to the transition state, with one imaginary frequency of the Hessian matrix corresponding to the vibrational mode along the intra-molecular proton transfer direction. For the case of the protonated Zundel, however, the geometry where the donor and acceptor atoms symmetrically share the proton corresponds to a minimum. Standard electronic structure methods are employed to perform these computations. Born-Oppenheimer potential energy surfaces for one-dimensional proton motion along the donor-acceptor axis are computed at these stationary point geometries. For that purpose, we choose a one-dimensional grid along the donor-acceptor axis with 2^N number of equally spaced grid points, symmetrically located about the stationary point (grid center). We perform electronic structure calculations at these points, on a classical computing platform, at the level of theory mentioned in Table I for the range of $N = 3$ to $N = 7$. Details of the electronic structure methods and total grid lengths for these potential energy surface calculations are provided in Table I.

B. Quantum simulation of proton-transfer dynamics in H_3O_2^- and Zundel using the mapping protocol

We examine the map by simulating the quantum dynamics of the water clusters and the ion-trap dynamics, on classical hardware, independently. For that, we choose the initial wavepacket state for the transferring proton in both systems in three different ways in the grid representation (x), the details of which are provided in Table II. The three initial wavepackets considered here are designed to probe a broad range of energy. The wavepacket, $\psi_L(x; 0)$ is particularly harsh given that it samples almost the full eigenspectrum, whereas the other two choices populate the lower regions of the energy spectrum. The corresponding Givens transformed wavepacket initial state is considered for time evolution

System	DA-distance	Level of theory	Grid Spread	No. of gridpoints
H_3O_2^-	2.42Å	CCSD/6-311++G(d,p)	0.66Å	8,16,32,64,128
H_5O_2^+	2.39Å	B3LYP/6-311++G(d,p)	0.66Å	8,16,32,64,128

TABLE I: Computational details for computing the potential energy surfaces for the transferring proton in both water clusters. In all cases the grid spacing ranges from 0.083Å (for 8 grid points, that is three qubits) to 0.005Å (for 128 grid points, that is 7 qubits). The finer grid spacings essentially approach the continuous limit given the mass of the proton and associated de Broglie wavelength. Also see Figure 7 for associated smoothness of potential.

Initial Wavepacket	Parameters	H_3O_2^-			H_5O_2^+		
		$ \langle\chi_0 \psi\rangle ^2$	E ^a	ϵ ^b	$ \langle\chi_0 \psi\rangle ^2$	E ^a	ϵ ^b
$\psi_L(x;0) = \delta(x - x_0)$	$x_0 = \text{donor site}$	0.27%	28.1	10^{-15}	0.08%	35.1	10^{-7}
$\psi_G(x;0) = \exp\left[-\frac{(x-\mu)^2}{2\sigma^2}\right]$	$\sigma = 0.1\text{Å}, \mu = 0.0\text{Å}$	87.7%	2.41	10^{-15}	93.71%	2.6	10^{-7}
$\psi_T(x;0) = \sum_j \exp[-E_j/kT]\chi_j(x)$	$T = 300K$	99%	1.34	10^{-15}	99.92%	1.92	10^{-7}

TABLE II: Parameters and characteristics of the initial wavepacket states considered for the transferring proton in the water cluster systems. The ground state, $|\chi_0\rangle$, overlap of for each $|\psi(x;0)\rangle$ and corresponding energy are reported for the case of $N = 3$. The mean absolute errors in probability, ϵ , computed between the classical propagated probability density, $\rho_C(x)$, and the probability density, $\rho_Q(x)$, computed using the mapping protocol in Section II, are provided.

^ain units of kcal/mol

^bas in Eq.(10)

using the block diagonal molecular Hamiltonian in the mapping protocol. Given the direct map described in Section II C between the permuted computational basis and the Givens transformed molecular grid basis, the initial wavepackets for the Ising Hamiltonian are chosen analogously to the initial wavepacket of the molecular system. The wavepacket state, $\psi_L(x;0)$, initialized on the end of the grid close to the donor site (as in Table II), corresponds to $\left\{\frac{|\tilde{x}_0\rangle - |\tilde{x}_7\rangle}{\sqrt{2}}\right\}$ in the Givens transformed basis. The corresponding initial state for the Ising Hamiltonian is chosen analogously to be $\left\{\frac{|\tilde{\lambda}_0\rangle - |\tilde{\lambda}_7\rangle}{\sqrt{2}}\right\}$ in the permuted computational basis, $\{|\tilde{\lambda}\rangle\}$. $\psi_G(x;0)$ and $\psi_T(x;0)$ are symmetric about the center of the grid and are mostly concentrated on the first block of the Givens transformed basis. The spin-lattice and molecular wavepackets are then independently propagated according to the transformed Ising and molecular Hamiltonians, and compared to gauge the accuracy of the quantum simulation.

Given the map between the matrix representation of the Ising Hamiltonian and the Givens transformed molecular Hamiltonian (in Eq. 4), as discussed in Ref. 137, the ion-trap hardware initial wavepacket state is directly propagated by the choice of $\{B_i^\gamma; J_{ij}^\gamma\}$ for arbitrary time-segments. The time-dependent probabilities resulting from the projection of the resultant time-dependent wavepacket on the computational basis, at each interval of time, are used to compute the difference between the

classical and quantum algorithms:

$$\epsilon = \frac{1}{T} \int dt \frac{1}{2^N} \int dx |\rho_Q(x) - \rho_C(x)| \quad (10)$$

where $\rho_Q(x)$ and $\rho_C(x)$ are the quantum and classical values of the wavepacket density, N is the number of qubits (ions), and T is the total simulation time. The resultant errors are provided in Table II.

Given the exact match between the spin-lattice dynamics and the quantum chemical dynamics, the features present in ion-trap dynamics must also exist in the chemical dynamics problem. Thus through the isomorphism constructed above, our algorithm allows the ability to extract properties of the chemical systems from the corresponding Ising Hamiltonian dynamics on the ion trap.

C. Quantum simulation of proton-transfer dynamics in H_3O_2^- and Zundel using Quantum Shannon Decomposition

The proton dynamics in the water clusters as simulated using the mapping protocol is exact for the case of $N = 3$. However, the number of gridpoints in that case does not capture the important characteristics of the potential energy surface as is clear from Figure 7. We therefore simulate the circuit decomposed unitary evolution of the proton wavepacket for more accurate representations of the chemical problem for $N = 3$ to 7 qubits. The unitary propagator, $e^{-i\hat{H}t/\hbar}$, for each value of t are decom-

Initial Wavepacket	ϵ (Eq. (10)) for H_5O_2^+					ϵ (Eq. (10)) for H_3O_2^-				
	$N = 3$	$N = 4$	$N = 5$	$N = 6$	$N = 7$	$N = 3$	$N = 4$	$N = 5$	$N = 6$	$N = 7$
$\psi_L(x; 0)$	6×10^{-4}	5×10^{-4}	4×10^{-4}	3×10^{-4}	2×10^{-4}	7×10^{-4}	5×10^{-4}	4×10^{-4}	3×10^{-4}	2×10^{-4}
$\psi_G(x; 0)$	6×10^{-4}	5×10^{-4}	4×10^{-4}	3×10^{-4}	2×10^{-4}	7×10^{-4}	5×10^{-4}	4×10^{-4}	3×10^{-4}	2×10^{-4}
$\psi_T(x; 0)$	6×10^{-4}	5×10^{-4}	4×10^{-4}	3×10^{-4}	2×10^{-4}	7×10^{-4}	5×10^{-4}	4×10^{-4}	3×10^{-4}	2×10^{-4}

TABLE III: The mean absolute errors in probability (Eq. (10)) computed between the classical propagated probability density $\rho_C(x)$ and the QASM simulated probability densities, $\rho_Q(x)$, using the circuit decomposition method summarized in Section III. The number of shots is 1000. Errors are reported for different initial nuclear wavepacket states of the transferring proton in both water clusters for all cases of $N = 3 - 7$. As the number of shots is increased, the error decreases as noted in Figure 8.

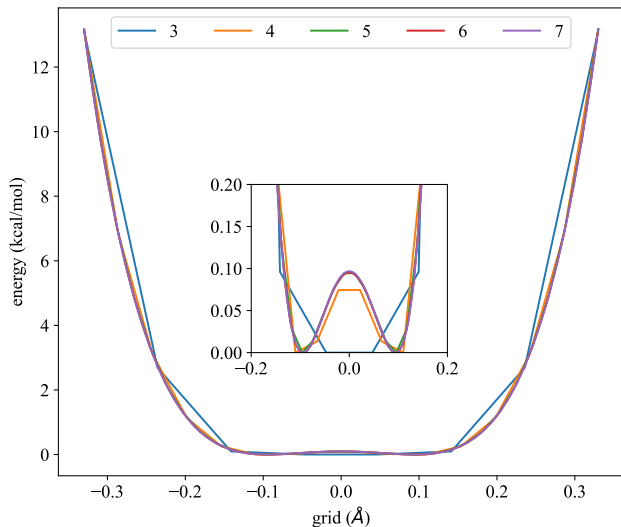


FIG. 7: The one-dimensional potential energy surfaces for the proton along the donor-acceptor axis in H_3O_2^- computed using a range of grid separations (refer Table I). The surfaces converge with increasing gridpoint densities (64 and 128 for $N = 6$ and $N = 7$ respectively). The low barrier height is shown in the inset for all grid point densities.

posed into a sequence of quantum gates using the Quantum Shannon decomposition method detailed in Section III. This decomposition will result in a significantly lower number of gates since the number of gates remains constant than in a Trotter-based decomposition where the circuit depth and gate counts double with subsequent Trotter steps. We implement the resulting quantum circuits on IBM’s QASM simulator using their software development kit, Qiskit. Probability densities are measured after unitary evolution at each time step. The errors in probability densities for the circuit implementation and classical propagation are computed using Eq. (10) and reported in Table III for the proton transfer dynamics in both the water clusters. Since the QASM simulator emulates the behavior of an actual quantum device, the precision of the estimated probabilities depends on the number of measurement shots used for each time step.

For about 1000 shots per time step, the error in the probabilities is of the order of 10^{-4} , across all qubit cases, as reported in Table III. We also report probability errors for an increasing number of measurement shots and see agreement up to 10^{-6} . Figure 8 shows how the error improves as we increase the number of shots from 10^3 to 10^6 for all qubit cases. Furthermore, we compute the Fourier transform of the measured time-evolved probability densities, $\rho_Q(x, t)$, which results in a spectrum with Fourier peaks corresponding to the frequency differences between the energy eigenvalues. The relevant details are provided in SI Section D. We can extract the oscillation frequencies of the shared proton in both chemical systems from these Fourier spectra of the frequency differences. In Figure 9, we compare the lower level eigenenergies obtained from the Fourier transform of the time-evolved probabilities on QASM to those obtained from the corresponding exact diagonalization for all bound eigenstates for both the chemical systems for qubit cases $N = 3 - 7$. The absolute errors between the QASM simulated eigen energies and the exact diagonalization results are well below 1 kcal/mol for the first four and three energy levels for H_5O_2^+ and H_3O_2^- , respectively. The errors in the frequency spectrum are not affected by the increase in the number of shots since the frequency resolution depends inversely on the total time of evolution, which is consistent for all cases considered here. An increase to 6–7 qubits, with a total time interval of several hundred femtoseconds and approximately 10^3 measurement shots, provides sufficient contrast in the measured probabilities to capture the relevant dynamics with accuracy beyond typical chemical or spectroscopic precision for hydrogen-bonded systems like those considered here.

V. CONCLUSIONS

The promise of solving exponentially complex problems efficiently using quantum computing hardware and associated quantum computing algorithms software is a rapidly evolving research frontier¹⁷². While we are in the early stages of this quantum revolution, there are a wide set of scientific and technological areas that can benefit from such developments. However, true progress in such areas can only be achieved by a rigorous study and un-

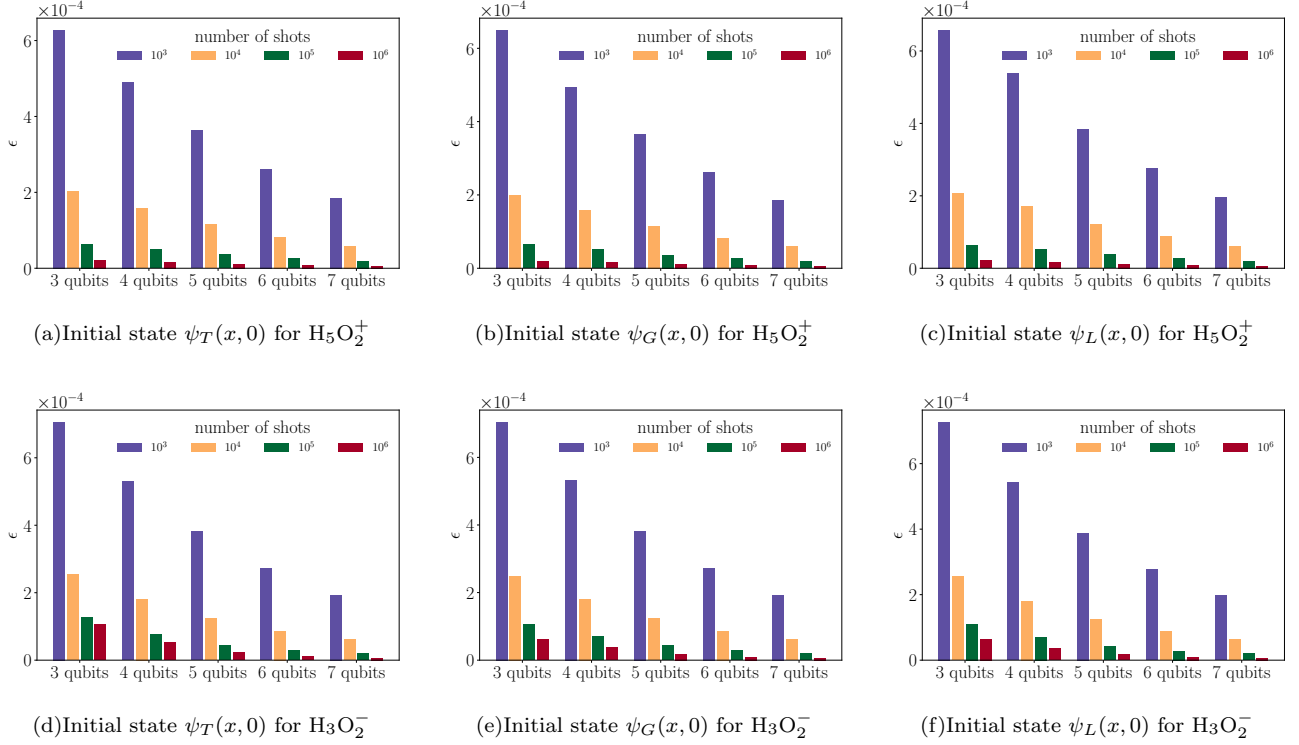


FIG. 8: Vertical axes show probability errors, (ϵ in Eq. (10)) for $N = 3 - 7$ qubits and for the different initial nuclear wavepacket states as a function of the number of measurement shots on IBM’s QASM simulator for both chemical systems. Clearly the error reduces drastically with increasing shots.

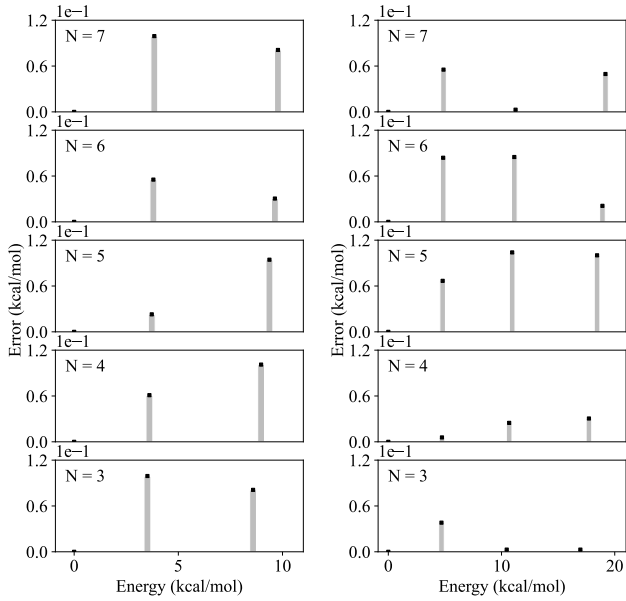


FIG. 9: Eigenenergy differences between the classically computed (exact diagonalization) and QASM computed eigenenergies for the first three and four eigenvalues for H_5O_2^+ (left) and H_3O_2^- (right).

understanding of the electronic structure and dynamics of complex materials, thus requiring accurate treatment of electron correlation effects in conjunction with a rigorous treatment of quantum nuclear effects^{57,62,63,186–189}.

In this paper, we discuss (a) the Hamiltonian mapping protocol detailed in Ref. 137 and (b) a quantum circuit method based on the Quantum Shannon decomposition for simulating quantum nuclear dynamics. Using the two methods discussed here we simulate the time evolution of the quantum nuclear wavepacket corresponding to the shared-proton degree of freedom in a short-strong hydrogen bond in small water clusters. The Hamiltonian mapping is a general but approximate mapping procedure between a quantum chemical dynamics problem, constructed on a single Born-Oppenheimer surface, and an ion-trap quantum simulator where the dynamics are dictated by a generalized form of a spin-lattice or Ising model Hamiltonian. This is exact for a small number of qubits while it becomes approximate for a larger number of qubits with quantitative error measures. The quantum circuit decomposition technique, on the other hand, is in principle exact for a higher number of qubits but practical implementation of the circuits remains a challenge on near-term quantum architectures due to the exponential increase in the number of entangling gates in the circuit decomposition.

The key step involved in facilitating our Hamiltonian

map is the partitioning of the coupled qubit space into two zones that we illustrate using the qsphere representation of the computational basis. Once the coupled qubit computational basis set is partitioned in such a way, the Ising model Hamiltonian reduces into a block form thus allowing the possibility to map all problems that may be written in a similar block form. The Quantum Shannon decomposition method, on the other hand, reduces any arbitrary unitary into a compact sequence of quantum gates from a universal gate set. The decomposition is also formally exact for an arbitrary dimensional unitary. This can also treat chemical problems with arbitrary potential energy surfaces and yields a number of entangling gates close to the expected theoretical lower bound.

We consider intra-molecular proton-transfers in hydroxide and protonated water clusters and show how such problems can be mapped to an ion-trap system, and also show that the dynamics can be simulated using a quantum circuit decomposition method on a quantum simulator. General quantum nuclear dynamics problems, however, have unsymmetric potential energy surfaces and are generally performed in higher dimensions. Critical extensions to higher quantum nuclear dimensions have been implemented using tensor networks in Refs. 140 and 139. The methods discussed here will become critical in extending our mapping protocol to general potentials in higher dimensions, as will be considered in future publications.

VI. ACKNOWLEDGMENTS

This research was supported by the National Science Foundation grants CHE-2102610 (SSI), OMA-1936353 (SSI and PR) and CHE-2311165 (SSI and PR).

- ¹ Shin, J.-W.; Hammer, N. I.; Diken, E. G.; Johnson, M. A.; Walters, R. S.; Jaeger, T. D.; Duncan, M. A.; Christie, R. A.; Jordan, K. D. Infrared Signature of Structures Associated with the $\text{H}^+(\text{H}_2\text{O})_n$ ($N = 6$ to 27) Clusters. *Science* **2004**, 304, 1137.
- ² Iyengar, S. S.; Petersen, M. K.; Day, T. J. F.; Burnham, C. J.; Teige, V. E.; Voth, G. A. The Properties of Ion-Water Clusters. I. the Protonated 21-Water Cluster. *J. Chem. Phys.* **2005**, 123, 084309.
- ³ Iyengar, S. S. Further Analysis of the Dynamically Averaged Vibrational Spectrum for the “magic” Protonated 21-Water Cluster. *J. Chem. Phys.* **2007**, 126, 216101.
- ⁴ Wu, C.-C.; Lin, C.-K.; Chang, H.-C.; Jiang, J.-C.; Kuo, J.-L.; Klein, M. L. Protonated Clathrate Cages Enclosing Neutral Water Molecules: $\text{H}^+(\text{H}_2\text{O})_{21}$ and $\text{H}^+(\text{H}_2\text{O})_{28}$. *J. Chem. Phys.* **2005**, 122, 074315.
- ⁵ Asthagiri, D.; Pratt, L. R.; Kress, J. D.; Gomez, M. A. Hydration and Mobility of $\text{HO}^-(\text{Aq})$. *Proc. Natl. Acad. Sci.* **2004**, 101, 7229.
- ⁶ Tuckerman, M. E.; Marx, D.; Parrinello, M. The Nature and Transport Mechanism of Hydrated Hydroxide Ions in Aqueous Solution. *Nature* **2002**, 417, 925.
- ⁷ Agmon, N. Mechanism of Hydroxide Mobility. *Chem. Phys. Lett.* **2000**, 319, 247.
- ⁸ Diken, E. G.; Headrick, J. M.; Roscioli, J. R.; Bopp, J. C.; Johnson, M. A.; McCoy, A. B. Fundamental Excitations of the Shared Proton in the H_3O_2^- and H_5O_2^+ Complexes. *J. Phys. Chem. A* **2005**, 109, 1487.
- ⁹ Robertson, W. H.; Diken, E. G.; Price, E. A.; Shin, J.-W.; Johnson, M. A. Spectroscopic Determination of the OH^- Solvation Shell in the $\text{OH}^-(\text{H}_2\text{O})_n$ Clusters. *Science* **2003**, 299, 1367.
- ¹⁰ Mundy, C. J.; Kuo, I.-F. W.; Tuckerman, M. E.; Lee, H.-S.; Tobias, D. J. Hydroxide anion at the air–water interface. *Chem. Phys. Lett.* **2009**, 481, 2.
- ¹¹ Miyazaki, M.; Fujii, A.; Ebata, T.; Mikami, N. Infrared Spectroscopic Evidence for Protonated Water Clusters Forming Nanoscale Cages. *Science* **2004**, 304, 1134.
- ¹² Xiao, X.-D.; Vogel, V.; Shen, Y. R. Probing the Proton Excess at Interfaces by Second Harmonic Generation. *Chem. Phys. Lett.* **1989**, 163, 555.
- ¹³ Radüge, C.; Pflumio, V.; Shen, Y. R. Surface Vibrational Spectroscopy of Sulphuric Acid-Water Mixtures at the Liquid-Vapour Interface. *Chem. Phys. Lett.* **1997**, 274, 140.
- ¹⁴ Achatz, U.; Fox, B. S.; Beyer, M. K.; Bondybey, V. E. Hypoiodous Acid As Guest Molecule in Protonated Water Clusters: A Combined FT-ICR/DFT Study of $\text{I}(\text{H}_2\text{O})_n^+$. *J. Am. Chem. Soc.* **2001**, 123, 6151.
- ¹⁵ Lee, S.-W.; Cox, H.; Goddard, I., W. A.; Beauchamp, J. L. Chemistry in Nanodroplets: Studies of Protonation Sites of Substituted Anilines in Water Clusters Using FT-ICR. *J. Am. Chem. Soc.* **2000**, 122, 9201.
- ¹⁶ Tuckerman, M. E.; Marx, D.; Klein, M. L.; Parrinello, M. On the Quantum Nature of the Shared Proton in Hydrogen Bonds. *Science* **1997**, 275, 817–820.
- ¹⁷ Tuckerman, M. E.; Laasonen, K.; Sprik, M.; Parrinello, M. Ab Initio Molecular Dynamics Simulation of the Solvation and Transport of H_3O^+ and OH^- . *J. Phys. Chem.* **1995**, 99, 5749.
- ¹⁸ Sadhukhan, S.; Munoz, D.; Adamo, C.; Scuseria, G. E. Predicting Proton Transfer Barriers with Density Functional Methods. *Chem. Phys. Lett.* **1999**, 306, 83.
- ¹⁹ Lobaugh, J.; Voth, G. A. The Quantum Dynamics of an Excess Proton in Water. *J. Chem. Phys.* **1996**, 104, 2056–.
- ²⁰ McEwan, M. J.; Phillips, L. F. *Chemistry of the Atmosphere*; Edward Arnold: London, 1975.
- ²¹ Wayne, R. P. *Chemistry of the Atmosphere*; Clarendon Press: Oxford, 1994.
- ²² McEwan, M. J.; Phillips, L. F. *Chemistry in the Upper Atmosphere*. *Accounts of Chemical Research* **1970**, 3, 9.
- ²³ Teeter, M. M. Water Structure of a Hydrophobic Protein at Atomic Resolution: Pentagon Rings of Water Molecules in Crystals of Crambin. *Proc. Natl. Acad. Sci. U.S.A.* **1984**, 81, 6014.
- ²⁴ Neidle, S.; Berman, H. M.; Shieh, H. S. Highly Structured Water Network in Crystals of a Deoxydinucleoside-Drug Complex. *Nature* **1980**, 288, 129.
- ²⁵ Lipscomb, L. A.; Peek, M. E.; Zhou, F. X.; Bertrand, J. A.; VanDerveer, D.; Williams, L. D. Water Ring Structure at Dna Interfaces - Hydration and Dynamics of Dna Anthracycline Complexes. *Biochemistry* **1994**, 33, 3649.
- ²⁶ Cleland, W. W.; Kreevoy, M. M. Low-Barrier Hydrogen-Bonds and Enzymatic Catalysis. *Science* **1994**, 264, 1887.
- ²⁷ Warshel, A.; Papazyan, A.; Kollman, P. A. *Science* **1995**, 269, 102.
- ²⁸ Marx, D.; Tuckerman, M. E.; Parrinello, M. Solvated Excess Protons in Water: Quantum Effects on the Hydration Structure. *J. Phys.: Condens. Matter* **2000**, 12, A153.
- ²⁹ Ricard, T. C.; Zhu, X.; Iyengar, S. S. Capturing weak interactions in surface adsorbate systems at coupled cluster accuracy: a graph-theoretic molecular fragmentation approach improved through machine learning. *J. Chem. Theory Comput.* **2023**, 19, 8541.
- ³⁰ Narayan, S.; Muldoon, J.; Finn, M.; Fokin, V.; Kolb, H.; Sharpless, K. “On Water”: Unique reactivity of organic compounds in aqueous suspension. *Angew. Chem.* **2005**, 44, 3275–3279.
- ³¹ Gajewski, J. The Claisen rearrangement. Response to solvents and substituents: The case for both hydrophobic and hydrogen bond acceleration in water and for a variable transition state. *Acc. Chem. Res.* **1997**, 30, 219–225.
- ³² Breslow, R.; Maitra, U.; Rideout, D. Selective Diels-Alder Reactions In Aqueous-Solutions And Suspensions. *Tetrahedron Lett.* **1983**, 24, 1901–1904.
- ³³ Breslow, R.; Maitra, U. On The Origin Of Product Selectivity In Aqueous Diels-Alder Reactions. *Tetrahedron Lett.* **1984**, 25, 1239–1240.
- ³⁴ Breslow, R. Hydrophobic Effects On Simple Organic-Reactions In Water. *Acc. Chem. Res.* **1991**, 24, 159–164.
- ³⁵ Dejong, P. H. K.; Wilson, J. E.; Neilson, G. W.; Buckingham, A. D. Hydrophobic Hydration Of Methane. *Mol. Phys.* **1997**, 91, 99–103.
- ³⁶ Chanda, A.; Fokin, V. V. Synthesis “On Water”. *Chem. Rev.* **2009**, 109, 725–748.
- ³⁷ Shapiro, N.; Vigalok, A. Highly Efficient Organic Reactions “On Water”, “In Water”, and both. *Angew. Chem.* **2008**, 47, 2849–2852.
- ³⁸ Huang, J.; Zhang, X.; Armstrong, D. W. Highly Efficient Asymmetric Direct Stoichiometric Aldol Reactions On/In Water. *Angew. Chem.* **2007**, 46, 9073–9077.

- ³⁹ Turner, G. L.; Morris, J. A.; Greaney, M. F. Direct Arylation Of Thiazoles On Water. *Angew. Chem.* **2007**, *46*, 7996–8000.
- ⁴⁰ Wu, X.; Li, X.; Zanotti-Gerosa, A.; Pettman, A.; Liu, J.; Mills, A. J.; Xiao, J. Rh(III)- And Ir(III)-Catalyzed Asymmetric Transfer Hydrogenation Of Ketones In Water. *Chemistry-A European Journal* **2008**, *14*, 2209–2222.
- ⁴¹ Butler, R. N.; Coyne, A. G.; Cunningham, W. J.; Moloney, E. M. Water And Organic Synthesis: A Focus On The In-Water And On-Water Border. Reversal Of The In-Water Breslow Hydrophobic Enhancement Of The Normal Endo-Effect On Crossing To On-Water Conditions For Huisgen Cycloadditions With Increasingly Insoluble Organic Liquid And Solid π -Dipolarophiles. *Journal Of Organic Chemistry* **2013**, *78*, 3276–3291.
- ⁴² Davis, J. G.; Rankin, B. M.; Gierszal, K. P.; Ben-Amotz, D. On The Cooperative Formation Of Non-Hydrogen-Bonded Water At Molecular Hydrophobic Interfaces. *Nat. Chem.* **2013**, *5*, 796–802.
- ⁴³ Jung, Y.; Marcus, R. A. On The Theory Of Organic Catalysis On Water. *J. Amer. Chem. Soc.* **2007**, *129*, 5492–5502.
- ⁴⁴ Jung, Y.; Marcus, R. A. Protruding Interfacial OH Groups And “On-Water” Heterogeneous Catalysis. *J. Phys. Condens. Matter* **2010**, *22*, 284117.
- ⁴⁵ Wang, Y.; Hodas, N. O.; Jung, Y.; Marcus, R. A. Microscopic Structure And Dynamics Of Air/Water Interface By Computer Simulations-Comparison With Sum-Frequency Generation Experiments. *Physical Chemistry Chemical Physics* **2011**, *13*, 5388–5393.
- ⁴⁶ Kuehne, T. D.; Pascal, T. A.; Kaxiras, E.; Jung, Y. New Insights Into The Structure Of The Vapor/Water Interface From Large-Scale First-Principles Simulations. *Journal of Physical Chemistry Letters* **2011**, *2*, 105–113.
- ⁴⁷ Karhan, K.; Khaliullin, R. Z.; Kuehne, T. D. On The Role Of Interfacial Hydrogen Bonds In “On-Water” Catalysis. *J. Chem. Phys.* **2014**, *141*, 22D528.
- ⁴⁸ Kessler, J.; Elgabarty, H.; Spura, T.; Karhan, K.; Partovi-Azar, P.; Hassanali, A. A.; Kuehne, T. D. Structure And Dynamics Of The Instantaneous Water/Vapor Interface Revisited By Path-Integral And Ab Initio Molecular Dynamics Simulations. *Journal of Physical Chemistry B* **2015**, *119*, 10079–10086.
- ⁴⁹ Schuster, M. F.; Meyer, W. H. Anhydrous Proton-Conducting Polymers. *Annu. Rev. Mat. Res.* **2003**, *33*, 233.
- ⁵⁰ Roscioli, J. R.; McCunn, L. R.; Johnson, M. A. Quantum Structure of the Intermolecular Proton Bond. *Science* **2007**, *316*, 249.
- ⁵¹ Moore, D. T.; Oomens, J.; van der Meer, L.; von Helden, G.; Meijer, G.; Valle, J.; Marshall, A. G.; Eyler, J. R. Probing the Vibrations of Shared, OH⁺O-Bound Protons in the Gas Phase. *ChemPhysChem* **2004**, *5*, 740.
- ⁵² Headrick, J. M.; Diken, E. G.; Walters, R. S.; Hammer, N. I.; Christie, R. A.; Cui, J.; Myshakin, E. M.; Duncan, M. A.; Johnson, M. A.; Jordan, K. Spectral Signatures of Hydrated Proton Vibrations in Water Clusters. *Science* **2005**, *308*, 1765.
- ⁵³ Valle, J. J.; Eyler, J. R.; Oomens, J.; Moore, D. T.; van der Meer, A. F. G.; von Helden, G.; Meijer, G.; Hendrickson, C. L.; Marshall, A. G.; Blakney, G. T. Free Electron Laser-Fourier Transform Ion Cyclotron Resonance Mass Spectrometry Facility for Obtaining Infrared Multiphoton Dissociation Spectra of Gaseous Ions. *Rev. Sci. Instr.* **2005**, *76*.
- ⁵⁴ Asmis, K. R.; Pivonka, N. L.; Santambrogio, G.; Brümmer, M.; Kaposta, C.; Neumark, D. M.; Wöste, L. Gas-Phase Infrared Spectrum of the Protonated Water Dimer. *Science* **2003**, *299*, 1375.
- ⁵⁵ Bush, M. F.; Forbes, M. W.; Jockusch, R. A.; Oomens, J.; Polfer, N. C.; Saykally, R.; Williams, E. Infrared Spectroscopy of Cationized Lysine and E-N-Methyl Lysine in the Gas Phase: Effects of Alkali Metal Ion Size and Proton Affinity on Zwitterion Stability. *J. Phys. Chem. A* **2007**, ASAP Article.
- ⁵⁶ Pivonka, N. L.; Kaposta, C.; Brummer, M.; von Helden, G.; Meijer, G.; Wöste, L.; Neumark, D. M.; Asmis, K. R. Probing a Strong Hydrogen Bond with Infrared Spectroscopy: Vibrational Predissociation of BrHBr⁻-Ar. *J. Chem. Phys.* **2003**, *118*, 5275.
- ⁵⁷ Nagel, Z.; Klinman, J. Tunneling and Dynamics in Enzymatic Hydride Transfer. *Chem. Revs.* **2006**, *106*, 3095.
- ⁵⁸ Soudackov, A. V.; Hammes-Schiffer, S. Probing Nonadiabaticity in the Proton-Coupled Electron Transfer Reaction Catalyzed by Soybean Lipoxygenase. *J. Phys. Chem. Lett.* **2014**, *5*, 3274.
- ⁵⁹ Hynes, J. T.; Klinman, J. P.; Limbach, H.-H.; Schowen, R. L., Eds. *Hydrogen-Transfer Reactions*; Wiley-VCH, Weinheim, Germany, 2007.
- ⁶⁰ Cukier, R. I.; Nocera, D. G. Proton-coupled electron transfer. *Ann. Rev. Phys. Chem.* **1998**, *49*, 337–369.
- ⁶¹ Mayer, J. M. Proton-coupled electron transfer: A Reaction Chemist’s View. *Ann. Rev. Phys. Chem.* **2004**, *55*, 363–390.
- ⁶² Iyengar, S. S.; Sumner, I.; Jakowski, J. Hydrogen Tunneling in an Enzyme Active Site: A Quantum Wavepacket Dynamical Perspective. *J. Phys. Chem. B* **2008**, *112*, 7601.
- ⁶³ Sumner, I.; Iyengar, S. S. Analysis of Hydrogen Tunneling in an Enzyme Active Site Using Von Neumann Measurements. *J. Chem. Theory Comput.* **2010**, *6*, 1698.
- ⁶⁴ Vendrell, O.; Gatti, F.; Meyer, H.-D. Dynamics and Infrared Spectroscopy of the Protonated Water Dimer. *Ang. Chem. Intl. Ed.* **2007**, *46*, 6918.
- ⁶⁵ Hammer, N. I.; Diken, E. G.; Roscioli, J. R.; Johnson, M. A.; Myshakin, E. M.; Jordan, K. D.; McCoy, A. B.; Huang, X.; Bowman, J. M.; Carter, S. The Vibrational Predissociation Spectra of the H₅O₂⁺-RG_n (RG = Ar, Ne) clusters: Correlation of the solvent perturbations in the free OH and shared proton transitions of the Zundel ion. *J. Chem. Phys.* **2005**, *122*, 244301.
- ⁶⁶ Hammerich, A. D.; Manthe, U.; Kosloff, R.; Meyer, H.; Cederbaum, L. S. Time-dependent photodissociation of methyl iodide with five active modes. *The Journal of Chemical Physics* **1994**, *101*, 5623–5646.
- ⁶⁷ Manthe, U.; Meyer, H. D.; Cederbaum, L. S. Wave-packet dynamics within the multiconfiguration Hartree framework: General aspects and application to NOCl. *J. Chem. Phys.* **1997**, *107*, 3199–3213.
- ⁶⁸ Beck, M. H.; Jäckle, A.; Worth, G. A.; Meyer, H.-D. The multiconfiguration time-dependent Hartree (MCTDH) method: a highly efficient algorithm for propagating wavepackets. *Phys. Rep.* **2000**, *324*, 1–105.
- ⁶⁹ Pasin, G.; Iung, C.; Gatti, F.; Meyer, H. D. Theoretical Investigation of Highly Excited Vibrational States in DFCO: Calculation of the Out-Of-Plane Bending States and Simulation of the Intramolecular Vibrational Energy

- Redistribution. *J. Chem. Phys.* **2007**, 126.
- ⁷⁰ Bowman, J. M. The Self-Consistent-Field Approach to Polyatomic Vibrations. *Acc. Chem. Res.* **1986**, 19, 202.
- ⁷¹ McCoy, A. B.; Gerber, R. B.; Ratner, M. A. A Quantitative Approximation for the Quantum Dynamics of Hydrogen Transfer: Transition State Dynamics and Decay in ClHCl^- . *J. Chem. Phys.* **1994**, 101, 1975.
- ⁷² Vendrell, O.; Gatti, F.; Meyer, H.-D. Full Dimensional (15D) Quantum-Dynamical Simulation of the Protonated Water-Dimer II: Infrared Spectrum and Vibrational Dynamics Dynamics and Infrared Spectroscopy of the Protonated Water Dimer. *J. Chem. Phys.* **2007**, 127, 184303.
- ⁷³ Vendrell, O.; Gatti, F.; Meyer, H.-D. Dynamics and Infrared Spectroscopy of the Protonated Water Dimer. *Angew. Chemie Intl. Ed.* **2007**, 46, 6918.
- ⁷⁴ Kaledin, M.; Kaledin, A. L.; Bowman, J. M. Vibrational Analysis of the H_5O_2^+ Infrared Spectrum Using Molecular and Driven Molecular Dynamics. *J. Phys. Chem. A* **2006**, 110, 2933.
- ⁷⁵ McCoy, A. B.; Huang, X.; Carter, S.; Bowman, J. M. Quantum Studies of the Vibrations in H_3O_2^- and D_3O_2^- . *J. Chem. Phys.* **2005**, 123, 064317.
- ⁷⁶ Pople, J. A.; Raghavachari, K.; Schlegel, H. B.; Binkley, J. S. Derivative Studies in Hartree-Fock and Møller-Plesset Theories. *Int. J. Quantum Chem., Quant. Chem. Symp.* **1979**, S13, 225–41.
- ⁷⁷ Pople, J. A.; Schlegel, H. B.; Raghavachari, K.; DeFrees, D. J.; Binkley, J. S.; Frisch, M. J.; Whiteside, R. A.; Hout, R. F.; Hehre, W. J. Molecular orbital studies of vibrational frequencies. *Int. J. Quantum Chem., Quant. Chem. Symp.* **1981**, S15, 269–278.
- ⁷⁸ Sumner, I.; Iyengar, S. S. Quantum Wavepacket *Ab Initio* Molecular Dynamics: An Approach for Computing Dynamically Averaged Vibrational Spectra Including Critical Nuclear Quantum Effects. *J. Phys. Chem. A* **2007**, 111, 10313.
- ⁷⁹ Li, X.; Oomens, J.; Eyler, J. R.; Moore, D. T.; Iyengar, S. S. Isotope Dependent, Temperature Regulated, Energy Repartitioning in a Low-Barrier, Short-Strong Hydrogen Bonded Cluster. *J. Chem. Phys.* **2010**, 132, 244301.
- ⁸⁰ Iyengar, S. S.; Parker, G. A.; Kouri, D. J.; Hoffman, D. K. Symmetry-Adapted Distributed Approximating Functionals: Theory and Application to the Rovibrational States of H_3^+ . *J. Chem. Phys.* **1999**, 110, 10283.
- ⁸¹ Vendrell, O.; Gatti, F.; Meyer, H.-D. Strong Isotope Effects in the Infrared Spectrum of the Zundel Cation. *Angew. Chem. Intl. Ed.* **2009**, 48, 352.
- ⁸² Schlegel, H. B.; Frisch, M. J. Computational bottlenecks in molecular orbital calculations. In *Theoretical and Computational Models for Organic Chemistry*; Springer, 1991; pp 5–33.
- ⁸³ Wyatt, R. E., Zhang, J. Z. H., Eds. *Dynamics of Molecules and Chemical Reactions*; Marcel Dekker Inc., New York, New York, 1996.
- ⁸⁴ Feynman, R. P.; Hibbs, A. R. *Quantum Mechanics and Path Integrals*; McGraw-Hill Book Company: New York, 1965.
- ⁸⁵ Meyer, H.-D.; Manthe, U.; Cederbaum, L. S. The multi-configurational time-dependent Hartree approach. *Chem. Phys. Lett.* **1990**, 165, 73–78.
- ⁸⁶ Nielsen, M. A.; Chuang, I. L. *Quantum computation and quantum information*; Cambridge University Press, Cambridge, 2000.
- ⁸⁷ Feynman, R. P.; Hey, J.; Allen, R. W. *Feynman Lectures on Computation*; Addison-Wesley Longman Publishing Co., Inc., 1998.
- ⁸⁸ Berman, L. The complexity of logical theories. *Theoretical Computer Science* **1980**, 11, 71–77.
- ⁸⁹ Deumens, E.; Diz, A.; Longo, R.; Öhrn, Y. Time-Dependent Theoretical Treatments of the Dynamics of Electrons and Nuclei in Molecular-Systems. *Rev. Mod. Phys.* **1994**, 66, 917.
- ⁹⁰ Kuppermann, A. The Geometric Phase in Reaction Dynamics. In *Dynamics of Molecules and Chemical Reactions*; Wyatt, R. E., Zhang, J. Z. H., Eds.; Marcel Dekker Inc., New York, New York, 1996; p 411.
- ⁹¹ Tal-Ezer, H.; Kosloff, R. An accurate and efficient scheme for propagating the time dependent Schrödinger equation. *J. Chem. Phys.* **1984**, 81, 3967.
- ⁹² Kouri, D. J.; Zhu, W.; Ma, X.; Pettitt, B. M.; Hoffman, D. K. *J. Phys. Chem.* **1992**, 96, 9622.
- ⁹³ Habershon, S.; Manolopoulos, D. E.; Markland, T. E.; Miller, T. F. Ring polymer molecular dynamics: Quantum effects in chemical dynamics from classical trajectories in an extended phase space. *Ann. Rev. Phys. Chem.* **2013**, 64, 387.
- ⁹⁴ DeGregorio, N.; Iyengar, S. S. Adaptive Dimensional Decoupling for Compression of Quantum Nuclear Wave Functions and Efficient Potential Energy Surface Representations through Tensor Network Decomposition. *J. Chem. Theory Comput.* **2019**, 15, 2780–2796.
- ⁹⁵ DeGregorio, N.; Iyengar, S. S. Efficient and Adaptive Methods for Computing Accurate Potential Surfaces for Quantum Nuclear Effects: Applications to Hydrogen-Transfer Reactions. *J. Chem. Theory Comput.* **2018**, 14, 30–47.
- ⁹⁶ Ayala, P.; Scuseria, G. Linear scaling second-order Møller-Plesset theory in the atomic orbital basis for large molecular systems. *J. Chem. Phys.* **1999**, 110, 3660.
- ⁹⁷ Schutz, M.; Werner, H. Low-order scaling local electron correlation methods. IV. Linear scaling local coupled-cluster (LCCSD). *J. Chem. Phys.* **2001**, 114, 661.
- ⁹⁸ Distasio, R. A., Jr.; Steele, R. P.; Rhee, Y. M.; Shao, Y.; Head-Gordon, M. An improved algorithm for analytical gradient evaluation in resolution-of-the-identity second-order Møller-Plesset perturbation theory: Application to alanine tetrapeptide conformational analysis. *J. Comput. Chem.* **2007**, 28, 839.
- ⁹⁹ Pavošević, F.; Pinski, P.; Riplinger, C.; Neese, F.; Valeev, E. F. SparseMaps—A systematic infrastructure for reduced-scaling electronic structure methods. IV. Linear-scaling second-order explicitly correlated energy with pair natural orbitals. *The Journal of Chemical Physics* **2016**, 144, 144109.
- ¹⁰⁰ Haycraft, C.; Li, J.; Iyengar, S. S. Efficient, “On-the-fly” Born–Oppenheimer and Car–Parrinello–type Dynamics with coupled cluster accuracy through Fragment Based Electronic Structure. *J. Chem. Theory Comput.* **2017**, 13, 21887.
- ¹⁰¹ Iyengar, S. S.; Kouri, D. J.; Hoffman, D. K. Particular and Homogeneous Solutions of Time-Independent Wavepacket Schrödinger Equations: Calculations Using a Subset of Eigenstates of Undamped or Damped Hamiltonians. *Theor. Chem. Acc.* **2000**, 104, 471.
- ¹⁰² Skone, J. H.; Pak, M. V.; Hammes-Schiffer, S. Nuclear-Electronic Orbital Nonorthogonal Configuration Interac-

- tion Approach. *J. Chem. Phys.* **2005**, 123, 134108.
- ¹⁰³ Iyengar, S. S.; Jakowski, J. Quantum Wavepacket Ab Initio Molecular Dynamics: An Approach to Study Quantum Dynamics in Large Systems. *J. Chem. Phys.* **2005**, 122, 114105.
- ¹⁰⁴ Binder, R.; Burghardt, I. First-principles description of intra-chain exciton migration in an oligo(para-phenylene vinylene) chain. II. ML-MCTDH simulations of exciton dynamics at a torsional defect. *The Journal of Chemical Physics* **2020**, 152, 204120.
- ¹⁰⁵ Kumar, A.; Iyengar, S. S. Fragment-based electronic structure for potential energy surfaces using a superposition of fragmentation topologies. *J. Chem. Theory Comput.* **2019**, 15, 5769.
- ¹⁰⁶ Abrams, D. S.; Lloyd, S. Simulation of many-body Fermi systems on a universal quantum computer. *Physical Review Letters* **1997**, 79, 2586.
- ¹⁰⁷ Aspuru-Guzik, A.; Dutoi, A. D.; Love, P. J.; Head-Gordon, M. Simulated quantum computation of molecular energies. *Science* **2005**, 309, 1704.
- ¹⁰⁸ Wang, H.; Kais, S.; Aspuru-Guzik, A.; Hoffmann, M. R. Quantum algorithm for obtaining the energy spectrum of molecular systems. *Physical Chemistry Chemical Physics* **2008**, 10, 5388–5393.
- ¹⁰⁹ Wecker, D.; Hastings, M. B.; Troyer, M. Progress towards practical quantum variational algorithms. *Physical Review A* **2015**, 92, 042303.
- ¹¹⁰ McClean, J. R.; Romero, J.; Babbush, R.; Aspuru-Guzik, A. The theory of variational hybrid quantum-classical algorithms. *New Journal of Physics* **2016**, 18, 023023.
- ¹¹¹ O’Malley, P. J. J.; Babbush, R.; Kivlichan, I. D.; Romero, J.; McClean, J. R.; Barends, R.; Kelly, J.; Roushan, P.; Tranter, A.; Ding, N.; Campbell, B.; Chen, Y.; Chen, Z.; Chiaro, B.; Dunsworth, A.; Fowler, A. G.; Jeffrey, E.; Lucero, E.; Megrant, A.; Mutus, J. Y.; Neeley, M.; Neill, C.; Quintana, C.; Sank, D.; Vainsencher, A.; Wenner, J.; White, T. C.; Coveney, P. V.; Love, P. J.; Neven, H.; Aspuru-Guzik, A.; Martinis, J. M. Scalable Quantum Simulation of Molecular Energies. *Phys. Rev. X* **2016**, 6, 031007.
- ¹¹² Parrish, R. M.; Hohenstein, E. G.; McMahan, P. L.; Martinez, T. J. Quantum Computation of Electronic Transitions Using a Variational Quantum Eigensolver. *Phys. Rev. Lett.* **2019**, 122, 230401.
- ¹¹³ Zhang, J. H.; Iyengar, S. S. Graph- $|Q\rangle\langle C|$: A Graph-based Quantum-classical algorithm for efficient electronic structure on hybrid quantum/classical hardware systems: Improved quantum circuit depth performance. *J. Chem. Theory Comput.* **2022**, 18, 2885.
- ¹¹⁴ Smart, S. E.; Mazziotti, D. A. Quantum solver of contracted eigenvalue equations for scalable molecular simulations on quantum computing devices. *Physical Review Letters* **2021**, 126, 070504.
- ¹¹⁵ Iyengar, S. S.; Saha, D.; Dwivedi, A.; Lopez-Ruiz, M. A.; Kumar, A.; Zhang, J. H.; Ricard, T. C.; Richerme, P.; Sabry, A. Quantum Algorithms for the Study of Electronic Structure and Molecular Dynamics: Novel Computational Protocols. In *Comprehensive Computational Chemistry*; Elsevier, 2023.
- ¹¹⁶ Iyengar, S. S.; Zhang, J. H.; Saha, D.; Ricard, T. C. Graph- $|Q\rangle\langle C|$: A Quantum Algorithm with Reduced Quantum Circuit Depth for Electronic Structure. *J. Phys. Chem. A* **2023**, 127, 9334.
- ¹¹⁷ Lanyon, B. P.; Whitfield, J. D.; Gillett, G. G.; Goggin, M. E.; Almeida, M. P.; Kassal, I.; Biamonte, J. D.; Mohseni, M.; Powell, B. J.; Barbieri, M.; Aspuru-Guzik, A.; White, A. G. Towards quantum chemistry on a quantum computer. *Nature chemistry* **2010**, 2, 106–111.
- ¹¹⁸ Lu, D.; Xu, N.; Xu, R.; Chen, H.; Gong, J.; Peng, X.; Du, J. Simulation of chemical isomerization reaction dynamics on a NMR quantum simulator. *Physical Review Letters* **2011**, 107, 020501.
- ¹¹⁹ Peruzzo, A.; McClean, J.; Shadbolt, P.; Yung, M.-H.; Zhou, X.-Q.; Love, P. J.; Aspuru-Guzik, A.; O’Brien, J. L. A variational eigenvalue solver on a photonic quantum processor. *Nat. Commun.* **2014**, 5, 4213.
- ¹²⁰ Kandala, A.; Mezzacapo, A.; Temme, K.; Takita, M.; Brink, M.; Chow, J. M.; Gambetta, J. M. Hardware-efficient variational quantum eigensolver for small molecules and quantum magnets. *Nature* **2017**, 549, 242.
- ¹²¹ Hempel, C.; Maier, C.; Romero, J.; McClean, J.; Monz, T.; Shen, H.; Jurcevic, P.; Lanyon, B. P.; Love, P.; Babbush, R.; Aspuru-Guzik, A.; Blatt, R.; Roos, C. F. Quantum Chemistry Calculations on a Trapped-Ion Quantum Simulator. *Phys. Rev. X* **2018**, 8, 031022.
- ¹²² Nam, Y.; Chen, J.-S.; Pisenti, N. C.; Wright, K.; Delaney, C.; Maslov, D.; Brown, K. R.; Allen, S.; Amini, J. M.; Apisdorf, J.; Beck, K. M.; Blinov, A.; Chaplin, V.; Chmielewski, M.; Collins, C.; Debnath, S.; Hudek, K. M.; Ducore, A. M.; Keesan, M.; Kreike-meier, S. M.; Mizrahi, J.; Solomon, P.; Williams, M.; Wong-Campos, J. D.; Moehring, D.; Monroe, C.; Kim, J. Ground-state energy estimation of the water molecule on a trapped-ion quantum computer. *npj Quantum Inf.* **2020**, 6, 33.
- ¹²³ Arute, F.; Arya, K.; Babbush, R.; Bacon, D.; Bardin, J. C.; Barends, R.; Boixo, S.; Broughton, M.; Buckley, B. B.; Buell, D. A.; Burkett, B.; Bushnell, N.; Chen, Y.; Chen, Z.; Chiaro, B.; Collins, R.; Courtney, W.; Demura, S.; Dunsworth, A.; Farhi, E.; Fowler, A.; Foxen, B.; Gidney, C.; Giustina, M.; Graff, R.; Habegger, S.; Harrigan, M. P.; Ho, A.; Hong, S.; Huang, T.; Huggins, W. J.; Ioffe, L.; Isakov, S. V.; Jeffrey, E.; Jiang, Z.; Jones, C.; Kafri, D.; Kechedzhi, K.; Kelly, J.; Kim, S.; Klimov, P. V.; Korotkov, A.; Kostritsa, F.; Landhuis, D.; Laptev, P.; Lindmark, M.; Lucero, E.; Martin, O.; Martinis, J. M.; McClean, J. R.; McEwen, M.; Megrant, A.; Mi, X.; Mohseni, M.; Mruczkiewicz, W.; Mutus, J.; Naaman, O.; Neeley, M.; Neill, C.; Neven, H.; Niu, M. Y.; O’Brien, T. E.; Ostby, E.; Petukhov, A.; Putterman, H.; Quintana, C.; Roushan, P.; Rubin, N. C.; Sank, D.; Satzinger, K. J.; Smelyanskiy, V.; Strain, D.; Sung, K. J.; Szalay, M.; Takeshita, T. Y.; Vainsencher, A.; White, T.; Wiebe, N.; Yao, Z. J.; Yeh, P.; Zalcman, A. Hartree-Fock on a superconducting qubit quantum computer. *Science* **2020**, 369, 1084–1089.
- ¹²⁴ Sparrow, C.; Martín-López, E.; Maraviglia, N.; Neville, A.; Harrold, C.; Carolan, J.; Joglekar, Y. N.; Hashimoto, T.; Matsuda, N.; O’Brien, J. L.; Tew, D. P.; Laing, A. Simulating the vibrational quantum dynamics of molecules using photonics. *Nature* **2018**, 557, 660–667.
- ¹²⁵ Wang, C. S.; Curtis, J. C.; Lester, B. J.; Zhang, Y.; Gao, Y. Y.; Freeze, J.; Batista, V. S.; Vaccaro, P. H.; Chuang, I. L.; Frunzio, L.; Jiang, L.; Girvin, S. M.; Schoelkopf, R. J. Efficient Multiphoton Sampling of Molecular Vibronic Spectra on a Superconducting Bosonic Processor. *Phys. Rev. X* **2020**, 10, 021060.

- ¹²⁶ Huh, J.; Guerreschi, G. G.; Peropadre, B.; McClean, J. R.; Aspuru-Guzik, A. Boson sampling for molecular vibronic spectra. *Nature Photonics* **2015**, *9*, 615–620.
- ¹²⁷ Wang, Y.; Sager-Smith, L. M.; Mazziotti, D. A. Quantum Simulation of Bosons with the Contracted Quantum Eigensolver. arXiv preprint arXiv:2307.07088 **2023**,
- ¹²⁸ Wang, C. S.; Frattini, N. E.; Chapman, B. J.; Puri, S.; Girvin, S. M.; Devoret, M. H.; Schoelkopf, R. J. Observation of Wave-Packet Branching through an Engineered Conical Intersection. *Phys. Rev. X* **2023**, *13*, 011008.
- ¹²⁹ Valahu, C. H.; Olaya-Agudelo, V. C.; MacDonell, R. J.; Navickas, T.; Rao, A. D.; Millican, M. J.; Pérez-Sánchez, J. B.; Yuen-Zhou, J.; Biercuk, M. J.; Hempel, C.; Tan, T. R.; Ivan, K. Direct observation of geometric-phase interference in dynamics around a conical intersection. *Nature Chemistry* **2023**, *15*, 1503–1508.
- ¹³⁰ Whitlow, J.; Jia, Z.; Wang, Y.; Fang, C.; Kim, J.; Brown, K. R. Quantum simulation of conical intersections using trapped ions. *Nature Chemistry* **2023**, *15*, 1509–1514.
- ¹³¹ Gambetta, F. M.; Zhang, C.; Henrich, M.; Lesanovsky, I.; Li, W. Exploring the many-body dynamics near a conical intersection with trapped Rydberg ions. *Physical Review Letters* **2021**, *126*, 233404.
- ¹³² Navickas, T.; MacDonell, R. J.; Valahu, C. H.; Olaya-Agudelo, V. C.; Scuccimarra, F.; Millican, M. J.; Matos, V. G.; Nourse, H. L.; Rao, A. D.; Biercuk, M. J.; Hempel, C.; Kassal, I.; Tan, T. R. Experimental Quantum Simulation of Chemical Dynamics. 2024; <https://arxiv.org/abs/2409.04044>.
- ¹³³ Wang, Y.; Mazziotti, D. A. Quantum simulation of conical intersections. *Physical Chemistry Chemical Physics* **2024**, *26*, 11491–11497.
- ¹³⁴ Xing, X.; Gomez Cadavid, A.; Izmaylov, A. F.; Tscherebul, T. V. A hybrid quantum-classical algorithm for multi-channel quantum scattering of atoms and molecules. *The Journal of Physical Chemistry Letters* **2023**, *14*, 6224–6233.
- ¹³⁵ Kale, S. S.; Kais, S. Simulation of Chemical Reactions on a Quantum Computer. *The Journal of Physical Chemistry Letters* **2024**, *15*, 5633–5642.
- ¹³⁶ Dietrick, S. M.; Iyengar, S. S. Constructing Periodic Phase Space Orbits from Ab Initio Molecular Dynamics Trajectories to Analyze Vibrational Spectra: Case Study of the Zundel (H_5O_2^+) Cation. *J. Chem. Theory and Comput.* **2012**, *8*, 4876.
- ¹³⁷ Saha, D.; Iyengar, S. S.; Richerme, P.; Smith, J. M.; Sabry, A. Mapping Quantum Chemical Dynamics Problems to Spin-Lattice Simulators. *J. Chem. Theory Comput.* **2021**, *17*, 6713–6732.
- ¹³⁸ Richerme, P.; Reville, M. C.; Yale, C. G.; Lobser, D.; Burch, A. D.; Clark, S. M.; Saha, D.; Lopez-Ruiz, M. A.; Dwivedi, A.; Smith, J. M.; et al., Quantum computation of hydrogen bond dynamics and vibrational spectra. *The Journal of Physical Chemistry Letters* **2023**, *14*, 7256–7263.
- ¹³⁹ Dwivedi, A.; Rasmussen, A. J.; Richerme, P.; Iyengar, S. S. Quantum nuclear dynamics on a distributed set of ion-trap quantum computing systems. *J. Am. Chem. Soc.* **2024**, In Press, <https://arxiv.org/abs/2406.05197>.
- ¹⁴⁰ Dwivedi, A.; Lopez-Ruiz, M. A.; Iyengar, S. S. Resource Optimization for Quantum Dynamics with Tensor Networks: Quantum and Classical Algorithms. *The Journal of Physical Chemistry A* **2024**, *128*, 6774–6797, PMID: 39101545.
- ¹⁴¹ Shende, V.; Bullock, S.; Markov, I. Synthesis of quantum-logic circuits. *IEEE Transactions on Computer-Aided Design of Integrated Circuits and Systems* **2006**, *25*, 1000–1010.
- ¹⁴² Cleland, W. W.; Kreevoy, M. M. *Science* **1994**, *264*, 1887.
- ¹⁴³ Chatfield, D. C.; Brooks, B. R. HIV-1 Protease Cleavage Mechanism Elucidated with Molecular Dynamics Simulation. *J. Am. Chem. Soc.* **1995**, *117*, 5561.
- ¹⁴⁴ Warshel, A.; Papazyan, A.; Kollman, P. A. On Low-Barrier Hydrogen-Bonds and Enzyme Catalysis. *Science* **1995**, *269*, 102.
- ¹⁴⁵ Perrin, C. L.; Nielson, J. B. 'Strong' Hydrogen Bonds in Chemistry and Biology. *Ann. Revs. of Phys. Chem.* **1997**, *48*, 511.
- ¹⁴⁶ Li, X.; Teige, V. E.; Iyengar, S. S. Can the Four-Coordinated, Penta-Valent Oxygen in Hydroxide Water Clusters Be Detected Through Experimental Vibrational Spectroscopy? *J. Phys. Chem. A* **2007**, *111*, 4815.
- ¹⁴⁷ Iyengar, S. S.; Li, X.; Sumner, I. The Study of Dynamically Averaged Vibrational Spectroscopy of Atmospherically Relevant Clusters Using Ab Initio Molecular Dynamics in Conjunction with Quantum Wavepackets. *Adv. Quant. Chem.* **2008**, *55*, 333.
- ¹⁴⁸ Hudson, B. S.; Verdal, N. Vibrational Dynamics in Short, Strong Symmetric Hydrogen Bonds: General Considerations and Two Examples. *Phys. B-Condensed Matter* **2006**, *385*, 212.
- ¹⁴⁹ Chisholm, C. R. I.; Haile, S. M. Entropy Evaluation of the Superprotonic Phase of CsHSO_4 : Pauling's Ice Rules Adjusted for Systems Containing Disordered Hydrogen-Bonded Tetrahedra. *Chemistry of Materials* **2007**, *19*, 270.
- ¹⁵⁰ Haile, S. M.; Chisholm, C. R. I.; Sasaki, K.; Boysen, D. A.; Uda, T. Solid Acid Proton Conductors: From Laboratory Curiosities to Fuel Cell Electrolytes. *Faraday Discussions* **2007**, *134*, 17.
- ¹⁵¹ Suzuki, K.; Hayashi, S. H-1 NMR Study of Proton Dynamics in $\text{Cs}_5\text{H}_3(\text{SO}_4)_4 \times \text{H}_2\text{O}$. *Phys. Rev. B* **2006**, *74*.
- ¹⁵² Olmschenk, S.; Younge, K. C.; Moehring, D. L.; Matsukevich, D. N.; Maunz, P.; Monroe, C. Manipulation and detection of a trapped Yb[^{sup +}] hyperfine qubit. *Phys. Rev. A* **2007**, *76*, 052314.
- ¹⁵³ Onsager, L. Crystal Statistics. I. A Two-Dimensional Model with an Order-Disorder Transition. *Phys. Rev.* **1944**, *65*, 117–149.
- ¹⁵⁴ McCoy, B. M.; Wu, T. T. *The Two-Dimensional Ising Model*; Harvard University Press: Cambridge, MA and London, England, 1973.
- ¹⁵⁵ Wilson, K. G. Renormalization Group and Critical Phenomena. I. Renormalization Group and the Kadanoff Scaling Picture. *Phys. Rev. B* **1971**, *4*, 3174–3183.
- ¹⁵⁶ Anderson, F. B.; Callen, H. B. Statistical Mechanics and Field-Induced Phase Transitions of the Heisenberg Antiferromagnet. *Phys. Rev.* **1964**, *136*, A1068–A1087.
- ¹⁵⁷ Cohen, E.; Tamir, B. D-Wave and predecessors: From simulated to quantum annealing. *International Journal of Quantum Information* **2014**, *12*, 1430002.
- ¹⁵⁸ Johnson, M. W.; Amin, M. H. S.; Gildert, S.; Lanting, T.; Hamze, F.; Dickson, N.; Harris, R.; Berkley, A. J.; Johansson, J.; Bunyk, P.; Chapple, E. M.; Enderud, C.; Hilton, J. P.; Karimi, K.; Ladizinsky, E.; Ladizinsky, N.; Oh, T.; Perminov, I.; Rich, C.; Thom, M. C.; Tolka-

- cheva, E.; Truncik, C. J. S.; Uchaikin, S.; Wang, J.; Wilson, B.; Rose, G. Quantum annealing with manufactured spins. *Nature* **2011**, 473, 194–198.
- ¹⁵⁹ Lechner, W.; Hauke, P.; Zoller, P. A quantum annealing architecture with all-to-all connectivity from local interactions. *Science Advances* **2015**, 1, e1500838.
- ¹⁶⁰ Xia, R.; Bian, T.; Kais, S. Electronic Structure Calculations and the Ising Hamiltonian. *J. Phys. Chem. B* **2018**, 122, 3384–3395.
- ¹⁶¹ Javadi-Abhari, A.; Treinish, M.; Krsulich, K.; Wood, C. J.; Lishman, J.; Gacon, J.; Martiel, S.; Nation, P. D.; Bishop, L. S.; Cross, A. W.; Johnson, B. R.; Gambetta, J. M. Quantum computing with Qiskit. 2024.
- ¹⁶² Kouri, D. J.; Huang, Y.; Hoffman, D. K. Iterated Real-Time Path Integral Evaluation Using a Distributed Approximating Functional Propagator and Average-Case Complexity Integration. *Phys. Rev. Lett.* **1995**, 75, 49.
- ¹⁶³ Hoffman, D. K.; Nayar, N.; Sharafeddin, O. A.; Kouri, D. J. Analytic Banded Approximation for the Discretized Free Propagator. *J. Phys. Chem.* **1991**, 95, 8299.
- ¹⁶⁴ Golub, G. H.; Van Loan, C. F. *Matrix computations*; JHU press, 2013; Vol. 3.
- ¹⁶⁵ Barenco, A.; Bennett, C. H.; Cleve, R.; DiVincenzo, D. P.; Margolus, N.; Shor, P.; Sleator, T.; Smolin, J. A.; Weinfurter, H. Elementary gates for quantum computation. *Physical review A* **1995**, 52, 3457.
- ¹⁶⁶ Möttönen¹, M.; Vartiainen, J. J. Decompositions of general quantum gates. *Trends in quantum computing research* **2006**, 149.
- ¹⁶⁷ Golub, G. H.; Loan, C. F. V. *Matrix Computations*; The Johns Hopkins University Press, Baltimore, 1996.
- ¹⁶⁸ Sutton, B. D. Computing the complete CS decomposition. *Numerical Algorithms* **2009**, 50, 33–65.
- ¹⁶⁹ Paige, C. C.; Wei, M. History and generality of the CS decomposition. *Linear Algebra and its Applications* **1994**, 208, 303–326.
- ¹⁷⁰ Möttönen, M.; Vartiainen, J. J.; Bergholm, V.; Salomaa, M. M. Quantum circuits for general multiqubit gates. *Physical review letters* **2004**, 93, 130502.
- ¹⁷¹ Chia, N.-H.; Chung, K.-M.; Lai, C.-Y. On the Need for Large Quantum Depth. *Proceedings of the 52nd Annual ACM SIGACT Symposium on Theory of Computing. STOC 2020*; New York, NY, USA, Association for Computing Machinery: New York, NY, USA, 2020; p 902–915.
- ¹⁷² Preskill, J. Quantum Computing in the NISQ era and beyond. *Quantum* **2018**, 2, 79.
- ¹⁷³ Baciou, L.; Michel, H. Interruption of the water chain in the reaction center from *Rhodobacter sphaeroides* reduces the rates of the proton uptake and of the second electron transfer to QB. *Biochemistry* **1995**, 34, 7967–7972.
- ¹⁷⁴ Guo, H.; Barnard, A. S. Proton transfer in the hydrogen-bonded chains of lepidocrocite: a computational study. *Phys. Chem. Chem. Phys.* **2011**, 13, 17864.
- ¹⁷⁵ Domene, C.; Sansom, M. S. Potassium channel, ions, and water: simulation studies based on the high resolution X-ray structure of KcsA. *Biophys. J.* **2003**, 85, 2787–2800.
- ¹⁷⁶ Mann, D. J.; Halls, M. D. Water Alignment and Proton Conduction inside Carbon Nanotubes. *Phys. Rev. Lett.* **2003**, 90, 195503.
- ¹⁷⁷ Song, W.; Joshi, H.; Chowdhury, R.; Najem, J. S.; Shen, Y.-X.; Lang, C.; Henderson, C. B.; Tu, Y.-M.; Farrell, M.; Pitz, M. E.; et al., Artificial water channels enable fast and selective water permeation through water-wire networks. *Nat. Nanotechnol.* **2020**, 15, 73–79.
- ¹⁷⁸ Hummer, G.; Rasaiah, J. C.; Noworyta, J. P. Water conduction through the hydrophobic channel of a carbon nanotube. *Nature* **2001**, 414, 188–190.
- ¹⁷⁹ Ye, Y.-S.; Rick, J.; Hwang, B.-J. Water soluble polymers as proton exchange membranes for fuel cells. *Polymers* **2012**, 4, 913–963.
- ¹⁸⁰ Tuckerman, M. E.; Ungar, P. J.; Vonrosenvinge, T.; Klein, M. L. Ab Initio Molecular Dynamics Simulations. *J. Phys. Chem.* **1996**, 100, 12878.
- ¹⁸¹ Tuckerman, M.; Laasonen, K.; Sprik, M.; Parrinello, M. *J. Phys. Chem.* **1995**, 99, 5749.
- ¹⁸² Schmitt, U. W.; Voth, G. A. The computer simulation of proton transport in water. *J. Chem. Phys.* **1999**, 111, 9361–9381.
- ¹⁸³ Schmitt, U. W.; Voth, G. A. Multistate empirical valence bond model for proton transport in water. *J. Phys. Chem. B* **1998**, 102, 5547–5551.
- ¹⁸⁴ Kemp, M. T.; Lewandowski, E. M.; Chen, Y. Low barrier hydrogen bonds in protein structure and function. *Biochimica et Biophysica Acta (BBA) - Proteins and Proteomics* **2021**, 1869, 140557.
- ¹⁸⁵ Frey, P. A.; Whitt, S. A.; Tobin, J. B. A Low-Barrier Hydrogen-Bond in the Catalytic Triad of Serine Proteases. *Science* **1994**, 264, 1927.
- ¹⁸⁶ Raghavachari, K.; Trucks, G. W.; Pople, J. A.; Head-Gordon, M. A fifth-order perturbation comparison of electron correlation theories. *Chem. Phys. Lett.* **1989**, 157, 479–483.
- ¹⁸⁷ Hammes-Schiffer, S. Theory of Proton-Coupled Electron Transfer in Energy Conversion Processes. *Acc. Chem. Res.* **2009**, 42, 1881–1889.
- ¹⁸⁸ Harris, D. F.; Lukoyanov, D. A.; Shaw, S.; Compton, P.; Tokmina-Lukaszewska, M.; Bothner, B.; Kelleher, N.; Dean, D. R.; Hoffman, B. M.; Seefeldt, L. C. The Mechanism of N₂ Reduction Catalyzed by Fe-Nitrogenase Involves Reductive Elimination of H₂. *Biochemistry* **2018**, 57, 701–710.
- ¹⁸⁹ Mardirossian, N.; Head-Gordon, M. Thirty years of density functional theory in computational chemistry: an overview and extensive assessment of 200 density functionals. *Molecular Physics* **2017**, 115, 2315–2372.

SUPPORTING INFORMATION

Quantum circuit and mapping algorithms for wavepacket dynamics: case study of anharmonic hydrogen bonds in protonated and hydroxide water clusters

Debadrita Saha,

*Department of Chemistry, and the Indiana University
Quantum Science and Engineering Center (IU-QSEC),
Indiana University, 800 E. Kirkwood Ave, Bloomington, IN-47405*

Philip Richerme

*Department of Physics, and the Indiana University Quantum Science and Engineering Center (IU-QSEC),
Indiana University, Bloomington, IN-47405*

Srinivasan S. Iyengar,

*Department of Chemistry, Department of Physics,
and the Indiana University Quantum Science and Engineering Center (IU-QSEC),
Indiana University, 800 E. Kirkwood Ave, Bloomington, IN-47405*

(Dated: December 6, 2024)

Here we discuss details regarding the unitary transforms that yield a block structure for the nuclear Hamiltonian and thus make the map between the ion-trap Hamiltonian and quantum nuclear Hamiltonian possible, electronic structure based potentials surfaces for H_3O_2^- and H_5O_2^+ , initial wavepacket details, a new correlation function based idea to compute vibrational eigenenergies, and more details on the vibrational spectra obtained from quantum simulations.

SI-1. UNITARY TRANSFORMATIONS THAT YIELD THE BLOCK STRUCTURE OF THE NUCLEAR HAMILTONIAN, FOR SYMMETRIC POTENTIALS, TO MAKE THESE COMMENSURATE WITH AND MAPPABLE TO THE SPIN-LATTICE HAMILTONIAN, \mathcal{H}_{IT}

The nuclear Hamiltonian, \mathcal{H}^{Mol} from Eq. (2) in the paper, has a banded Toeplitz structure due to the kinetic energy being expressed in terms of DAFs. The unitary transform that leads to the block structure of the nuclear Hamiltonian, similar to the structure of the Ising Hamiltonian, can be expressed as a product of Givens rotations. The effect of the Givens rotations on the grid basis states is to create symmetric and anti-symmetric superpositions of pairs of grid basis states that

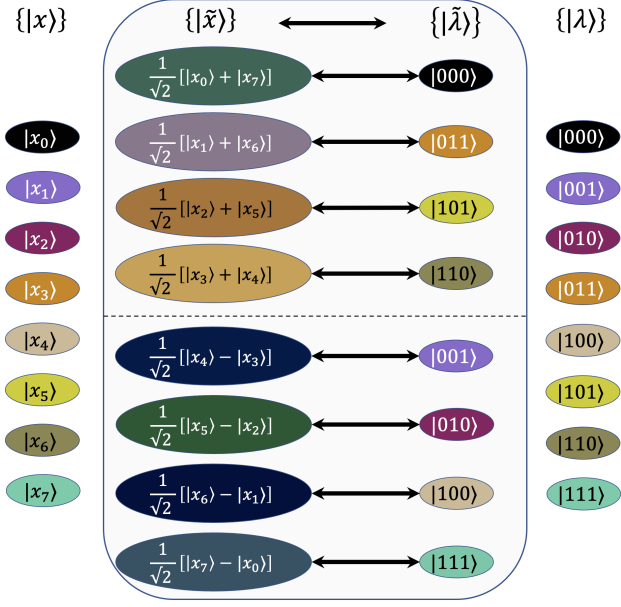


FIG. SI-1. An illustration of the mapping of the Givens transformed grid basis state representation, $|\tilde{x}\rangle$ (Eq. (SI-2)), for the discrete quantum nuclear Hamiltonian to the permuted computational basis state representation, $|\tilde{\lambda}\rangle$ (Section IIA in paper), for the Ising model Hamiltonian. The respective basis states map shown here for the case of 3 qubits holds true and can be generalized to an arbitrary number of qubits. The dashed line in the middle separates the two blocks of each Hamiltonian.

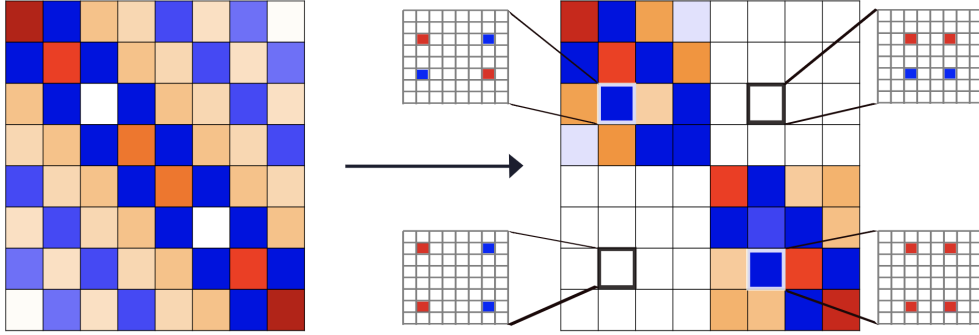


FIG. SI-2. An illustration of the block-diagonalization of the nuclear Hamiltonian, as captured by Eq. (SI-3). The original Hamiltonian, \mathcal{H}^{Mol} is on the left, whereas the transformed $\tilde{\mathcal{H}}^{Mol}$ is shown on the right. On the right side, specific matrix elements from each block of $\tilde{\mathcal{H}}_{il}^{Mol}$ are highlighted to illustrate Eqs. (SI-4) and (SI-5). These highlighted elements of $\tilde{\mathcal{H}}_{il}^{Mol}$ are obtained by combining elements of \mathcal{H}^{Mol} , as per Eq. (SI-3), and these are marked using red and blue squares in zoomed in representations matrix elements in \mathcal{H}^{Mol} . The blue (negative) and red (positive) indicate the phase of the corresponding elements of \mathcal{H}^{Mol} , as obtained from α_i in Eqs. (SI-3), (SI-4) and (SI-5).

are reflections about the grid center. To explain this, we introduce a uniform one-dimensional set

of grid points, $\{|x_i\rangle\}$ where $i \in (0, n)$, such that the Givens transformed grid basis, $\{|\tilde{x}_i\rangle\}$, may be represented as

$$|\tilde{x}_i\rangle \equiv \frac{1}{\sqrt{2}} [|x_i\rangle + |x_{n-i}\rangle], \quad 0 \leq i < (n+1)/2 \quad (\text{SI-1})$$

$$\equiv \frac{1}{\sqrt{2}} [|x_i\rangle - |x_{n-i}\rangle], \quad (n+1)/2 \leq i \leq n \quad (\text{SI-2})$$

where $n = 2^N - 1$. The grid basis and the Givens transformed grid basis, for a three-qubit system, are represented on the left columns of Figure SI-1. Equations SI-1 and SI-2 form two mutually orthogonal subspaces and are represented in the top and bottom portions of Figure SI-1, separated by the dashed line. These subspaces block diagonalize the nuclear Hamiltonian for symmetric potentials. This process is illustrated for a three-qubit system (2^3 -grid points) in Figure SI-2.

The i^{th} matrix element of the resultant molecular Hamiltonian in the Givens transformed grid basis is explicitly written as

$$\begin{aligned} \tilde{\mathcal{H}}_{il}^{Mol} = \frac{1}{2} \left(\mathcal{H}_{i,l}^{Mol} + \alpha_l \mathcal{H}_{i,n-l}^{Mol} + \alpha_i \mathcal{H}_{n-i,l}^{Mol} + \right. \\ \left. \alpha_i \alpha_l \mathcal{H}_{n-i,n-l}^{Mol} \right), \end{aligned} \quad (\text{SI-3})$$

where $\alpha_i = \text{sgn}[i - (n/2)]$. The elements of the diagonal blocks of $\tilde{\mathcal{H}}^{Mol}$ (matrix on the right in Figure (SI-2)) are obtained from Eq. (SI-3) as

$$\begin{aligned} \tilde{\mathcal{H}}_{il}^{Mol} &= \frac{1}{2} \left(\mathcal{H}_{i,l}^{Mol} + \alpha_i \mathcal{H}_{i,n-l}^{Mol} + \alpha_i \mathcal{H}_{n-i,l}^{Mol} + \right. \\ &\quad \left. \mathcal{H}_{n-i,n-l}^{Mol} \right) \\ &= [K(x_i, x_l) + \alpha_i K(x_i, x_{n-l})] + \\ &\quad \frac{1}{2} [V(x_i) + V(x_{n-l})] \delta_{i,l} \end{aligned} \quad (\text{SI-4})$$

The elements of the unitary transform, α_i are, in fact, the characters of the C_s point group. The right hand side of the above equation, therefore, represents a symmetry adapted transformation of the nuclear Hamiltonian, and the term $\frac{1}{2} [V(x_i) + V(x_{n-i})]$, symmetrizes the potential energy surface in one-dimension. By extension, for the elements of the off-diagonal blocks of $\tilde{\mathcal{H}}^{Mol}$ in Figure SI-2, $\alpha_l = -\alpha_i$ and

$$\begin{aligned} \tilde{\mathcal{H}}_{il}^{Mol} &= \frac{1}{2} \left(\mathcal{H}_{i,l}^{Mol} - \alpha_i \mathcal{H}_{i,n-l}^{Mol} + \alpha_i \mathcal{H}_{n-i,l}^{Mol} - \right. \\ &\quad \left. \mathcal{H}_{n-i,n-l}^{Mol} \right) \\ &= \frac{1}{2} [V(x_i) - V(x_{n-l})] \delta_{i,n-l} \end{aligned} \quad (\text{SI-5})$$

where the kinetic energy contribution is identically zero due to the Toeplitz nature of the kinetic energy operator (Eq. (2) in the paper), and only the anti-symmetric portion of the potential, $\frac{1}{2} [V(x_i) - V(x_{n-l})]$, contributes to the anti-diagonal part of $\tilde{\mathcal{H}}^{Mol}$. Thus for symmetric potentials such as those considered here, Eq. (SI-5) is identically zero. This observation becomes useful for our approach here.

**SI-2. ROLE OF GRID SPACING AND ELECTRONIC STRUCTURE THEORY IN THE
COMPUTATION OF POTENTIAL ENERGY SURFACES FOR THE PROTON
TRANSFER IN H_3O_2^- AND H_5O_2^+**

The level of theory used for the computation of potential energy surfaces for the two systems is CCSD/6-311++G(d,p) and B3LYP/6-311++G(d,p) respectively, as given in Table I of the paper. Here, we present the potential energy surfaces as computed using a hierarchy of electronic structure theories to justify the use of a higher level of theory (CCSD) for H_3O_2^- . The level of theory helped to capture the anharmonicities in the potential for H_3O_2^- . As can be observed from the figures below the MP2 surface develops a slight barrier height for $\Delta x = 0.021\text{\AA}$, while the barrier height is significant for the CCSD surface with $\Delta x = 0.044\text{\AA}$. The anharmonic nature of the CCSD surface is not captured for the case of $\Delta x = 0.094\text{\AA}$ implying that the width of the barrier is smaller than the grid spacing Δx .

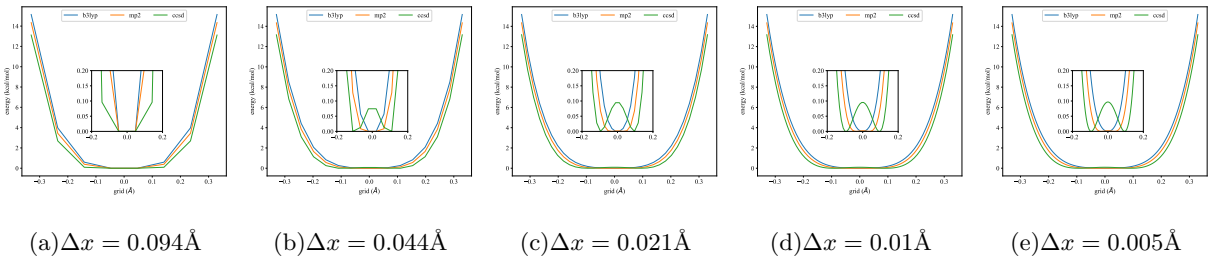


FIG. SI-3. The potential energy surface for the proton in H_3O_2^- as computed with a hierarchy of electronic structure methods (along with basis set 6-311++G(d,p)) for a range of grid spacing (Δx). The grid length is chosen to be 0.66\AA (recorded in Table I of the paper) and 2^N grid points for an increasing number of qubits $N = 3$ to 7 are chosen for (a)-(e).

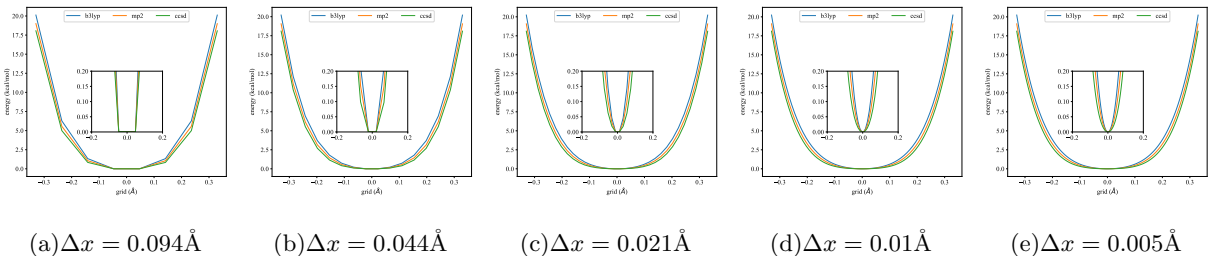


FIG. SI-4. The potential energy surface for the proton in H_5O_2^+ as computed with a hierarchy of electronic structure methods (along with basis set 6-311++G(d,p)) for a range of grid spacing (Δx). The grid length is chosen to be 0.66\AA (recorded in Table I of the paper) and 2^N grid points for an increasing number of qubits $N = 3$ to 7 are chosen for (a)-(e).

**SI-3. CHARACTERISTICS OF INITIAL WAVEPACKET STATES FOR THE
QUANTUM NUCLEI FOR QUANTUM DYNAMICS USING CIRCUIT
DECOMPOSITION**

H_3O_2^-		$ \langle \chi_0 \psi \rangle ^2$				E(kcal/mol)			
$\psi(x; 0)$	Parameters	$N = 4$	$N = 5$	$N = 5$	$N = 7$	$N = 4$	$N = 5$	$N = 6$	$N = 7$
$\psi_L(x; 0)$	$x_0 = \text{donor site}$	0.07%	0.01%	0.002%	0.0003%	82.1	307.6	1229.4	4955.4
$\psi_G(x; 0)$	$\sigma = 0.1\text{\AA}, \mu = 0.0\text{\AA}$	88.3%	88.9%	89.3%	89.6%	2.46	2.47	2.52	2.42
$\psi_T(x; 0)$	$T = 300K$	99.5%	99.6%	99.7%	99.7%	1.65	2.50	5.55	16.85
H_5O_2^+		$ \langle \chi_0 \psi \rangle ^2$				E(kcal/mol)			
$\psi(x; 0)$	Parameters	$N = 4$	$N = 5$	$N = 5$	$N = 7$	$N = 4$	$N = 5$	$N = 6$	$N = 7$
$\psi_L(x; 0)$	$x_0 = \text{donor site}$	0.03%	0.006%	0.0009%	0.0001%	89.16	314.70	1236.43	4962.46
$\psi_G(x; 0)$	$\sigma = 0.1\text{\AA}, \mu = 0.0\text{\AA}$	93.84%	94.03%	94.17%	94.26%	2.7	2.72	2.78	2.68
$\psi_T(x; 0)$	$T = 300K$	99.93%	99.94%	99.94%	99.94%	2.06	2.22	2.82	4.77

TABLE SI-1. Parameters and characteristics of the initial wavepacket states considered for the transferring proton in the water cluster systems. The ground state overlap and corresponding energy correspond to the cases of $N = 4 - 7$.

**SI-4. CALCULATION OF VIBRATIONAL PROPERTIES FROM FOURIER
TRANSFORMS OF THE TIME DYNAMICS OF THE SHARED NUCLEI**

To extract the oscillation frequencies of the shared-proton wavepacket in our hydrogen-bonded system, we perform a Fourier transform of the measured time-evolution data for the Zundel and hydroxide water cluster. Mathematically, this operation is equivalent to computing

$$\begin{aligned}
 \int e^{i\omega t} |\chi(x, t)|^2 dt &= \sum_{i,j} \left[\int e^{i\omega t} e^{i(E_j - E_i)t/\hbar} dt \right] c_j^* c_i \phi_j^*(x) \phi_i(x) \\
 &= \sum_{i,j} \delta(\omega - (E_j - E_i)/\hbar) c_j^* c_i \phi_j^*(x) \phi_i(x), \tag{SI-6}
 \end{aligned}$$

where the wavepacket $\chi(x, t)$ is expressed as a linear combination of eigenstates. This produces peaks in the Fourier spectrum corresponding to frequency differences between energy eigenstates, $(E_j - E_i)/\hbar$. This expression is also related to the Fourier transform of the density matrix auto-correlation function, $\text{Tr}[\rho(0)\rho(t)]$ as discussed below. The time-dependent density matrix in an

	ϵ (Eq.(9)) for H_5O_2^+ (shots= 10^4)					ϵ (Eq.(9)) for H_3O_2^- (shots= 10^4)				
$\psi(x;0)$	$N=3$	$N=4$	$N=5$	$N=6$	$N=7$	$N=3$	$N=4$	$N=5$	$N=6$	$N=7$
$\psi_L(x;0)$	2×10^{-4}	2×10^{-4}	1×10^{-4}	9×10^{-5}	6×10^{-5}	2×10^{-4}	2×10^{-4}	1×10^{-4}	9×10^{-5}	6×10^{-5}
$\psi_G(x;0)$	2×10^{-4}	2×10^{-4}	1×10^{-4}	8×10^{-5}	6×10^{-5}	2×10^{-4}	2×10^{-4}	1×10^{-4}	9×10^{-4}	6×10^{-4}
$\psi_T(x;0)$	2×10^{-4}	2×10^{-4}	1×10^{-4}	8×10^{-5}	6×10^{-5}	3×10^{-4}	2×10^{-4}	1×10^{-4}	9×10^{-5}	6×10^{-5}
	ϵ (Eq.(9)) for H_5O_2^+ (shots= 10^5)					ϵ (Eq.(9)) for H_3O_2^- (shots= 10^5)				
$\psi(x;0)$	$N=3$	$N=4$	$N=5$	$N=6$	$N=7$	$N=3$	$N=4$	$N=5$	$N=6$	$N=7$
$\psi_L(x;0)$	6×10^{-5}	5×10^{-5}	4×10^{-5}	3×10^{-5}	2×10^{-5}	1×10^{-4}	7×10^{-5}	4×10^{-5}	3×10^{-5}	2×10^{-5}
$\psi_G(x;0)$	6×10^{-5}	5×10^{-5}	4×10^{-5}	3×10^{-5}	2×10^{-5}	1×10^{-4}	7×10^{-5}	4×10^{-5}	3×10^{-5}	2×10^{-5}
$\psi_T(x;0)$	6×10^{-5}	5×10^{-5}	4×10^{-5}	3×10^{-5}	2×10^{-5}	1×10^{-4}	8×10^{-5}	4×10^{-5}	3×10^{-5}	2×10^{-5}
	ϵ (Eq.(9)) for H_5O_2^+ (shots= 10^6)					ϵ (Eq.(9)) for H_3O_2^- (shots= 10^6)				
$\psi(x;0)$	$N=3$	$N=4$	$N=5$	$N=6$	$N=7$	$N=3$	$N=4$	$N=5$	$N=6$	$N=7$
$\psi_L(x;0)$	2×10^{-5}	2×10^{-5}	1×10^{-5}	9×10^{-6}	6×10^{-6}	6×10^{-5}	4×10^{-5}	2×10^{-5}	1×10^{-5}	6×10^{-6}
$\psi_G(x;0)$	2×10^{-5}	2×10^{-5}	1×10^{-5}	8×10^{-6}	6×10^{-6}	6×10^{-5}	4×10^{-5}	2×10^{-5}	1×10^{-5}	6×10^{-6}
$\psi_T(x;0)$	2×10^{-5}	2×10^{-5}	1×10^{-5}	8×10^{-6}	6×10^{-6}	2×10^{-4}	5×10^{-5}	2×10^{-5}	1×10^{-6}	7×10^{-6}

TABLE SI-2. The mean absolute errors in probability (Eq. (9)) computed between the classical propagated probability density $\rho_C(x)$ and the QASM simulated probability densities, $\rho_Q(x)$, using the circuit decomposition method summarized in the main article. The number of shots used are 10^4 , 10^5 , and 10^6 respectively. Errors are reported for different initial nuclear wavepacket states of the transferring proton in both water clusters for all cases of $N = 3 - 7$. As the number of shots is increased, the error decreases as noted in Figure 8 in the paper.

eigenstate representation is given by,

$$\begin{aligned}
\rho(t) &= |\chi(t)\rangle \langle \chi(t)| = e^{-i\mathcal{H}t/\hbar} |\chi(0)\rangle \langle \chi(0)| e^{i\mathcal{H}t/\hbar} \\
&= \sum_{i,j} c_i(0) c_j^*(0) e^{-i\mathcal{H}t/\hbar} |\phi_i\rangle \langle \phi_j| e^{i\mathcal{H}t/\hbar} \\
&= \sum_{i,j} c_i(0) c_j^*(0) e^{i(E_i - E_j)t/\hbar} |\phi_i\rangle \langle \phi_j|, \tag{SI-7}
\end{aligned}$$

and is used to construct the Fourier transform of the density-density time auto-correlation function, $\text{Tr}[\rho(0)\rho(t)]$ as

$$\begin{aligned}
\int_{-\infty}^{+\infty} dt e^{i\omega t} \text{Tr}[\rho(0)\rho(t)] &= \int_{-\infty}^{+\infty} dt e^{i\omega t} \text{Tr} \left[|\chi(0)\rangle \langle \chi(0)| \sum_{i,j} c_i(0) c_j^*(0) e^{i(E_i - E_j)t/\hbar} |\phi_i\rangle \langle \phi_j| \right] \\
&= \sum_{i,j} |c_i(0)|^2 |c_j(0)|^2 \delta(\omega - (E_i - E_j)/\hbar), \tag{SI-8}
\end{aligned}$$

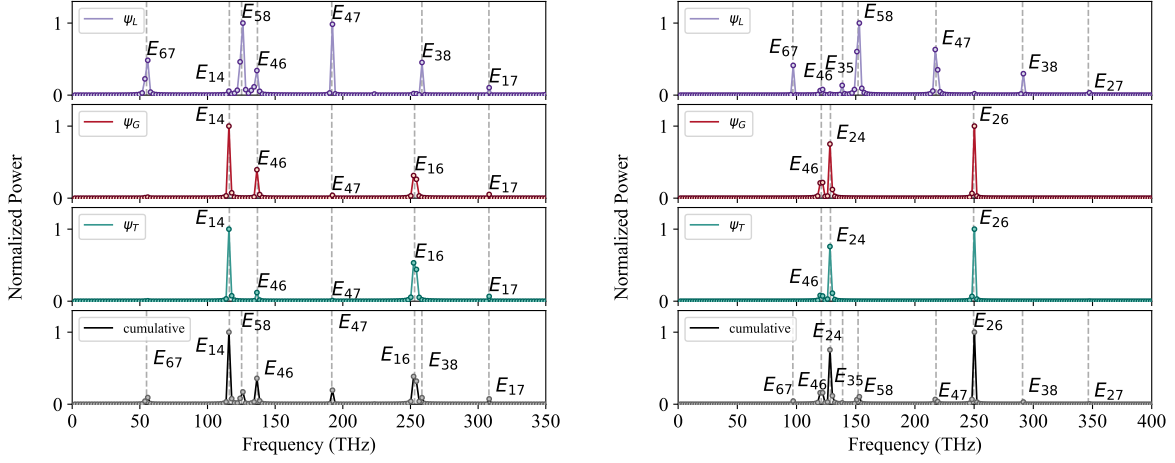


FIG. SI-5. The Fourier spectra showing all possible vibrational frequencies (as in equation SI-6) for the proton dynamics in the hydroxide (left) and protonated Zundel (right) water cluster corresponding to the different initial wavepackets given in Table SI-1 as obtained from the mapping algorithm. The dashed lines in gray are computed from the exact diagonalization of the Hamiltonian corresponding to $N = 3$.

which is further reduced the following using the convolution theorem,

$$\int dx \left| \int_{-\infty}^{+\infty} dt e^{i\omega t} \sum_{i,j} c_i(0) c_j^*(0) e^{i(E_i - E_j)t/\hbar} \phi_i(x) \phi_j(x) \right|^2 + \int dx dx' \left| \int_{-\infty}^{+\infty} dt e^{i\omega t} \sum_{i,j} c_i(0) c_j^*(0) e^{i(E_i - E_j)t/\hbar} \phi_i(x) \phi_j(x') \right|^2 \quad (\text{SI-9})$$

Note that the term on the first line of Eq. (SI-9), that is

$$\begin{aligned} \mathcal{I}(\omega; x) &= \int_{-\infty}^{+\infty} dt e^{i\omega t} \sum_{i,j} c_i(0) c_j^*(0) e^{i(E_i - E_j)t/\hbar} \phi_i(x) \phi_j(x) \\ &= \sum_{i,j} \delta(\omega - (E_i - E_j)) c_i(0) c_j^*(0) \phi_i(x) \phi_j(x), \end{aligned} \quad (\text{SI-10})$$

is identical to Eq. SI-6 which makes the first term in Eq. SI-9,

$$\mathcal{P}(\omega) = \int dx |\mathcal{I}(\omega; x)|^2 \quad (\text{SI-11})$$

While standard (classical) approaches may compute the results from Eq. (SI-9), a quantum computer can obtain information at a finer resolution and compute the individual terms inside the integral as shown in Eq. (SI-10) separately. Figures SI-5 and SI-6 show the Fourier transforms of the

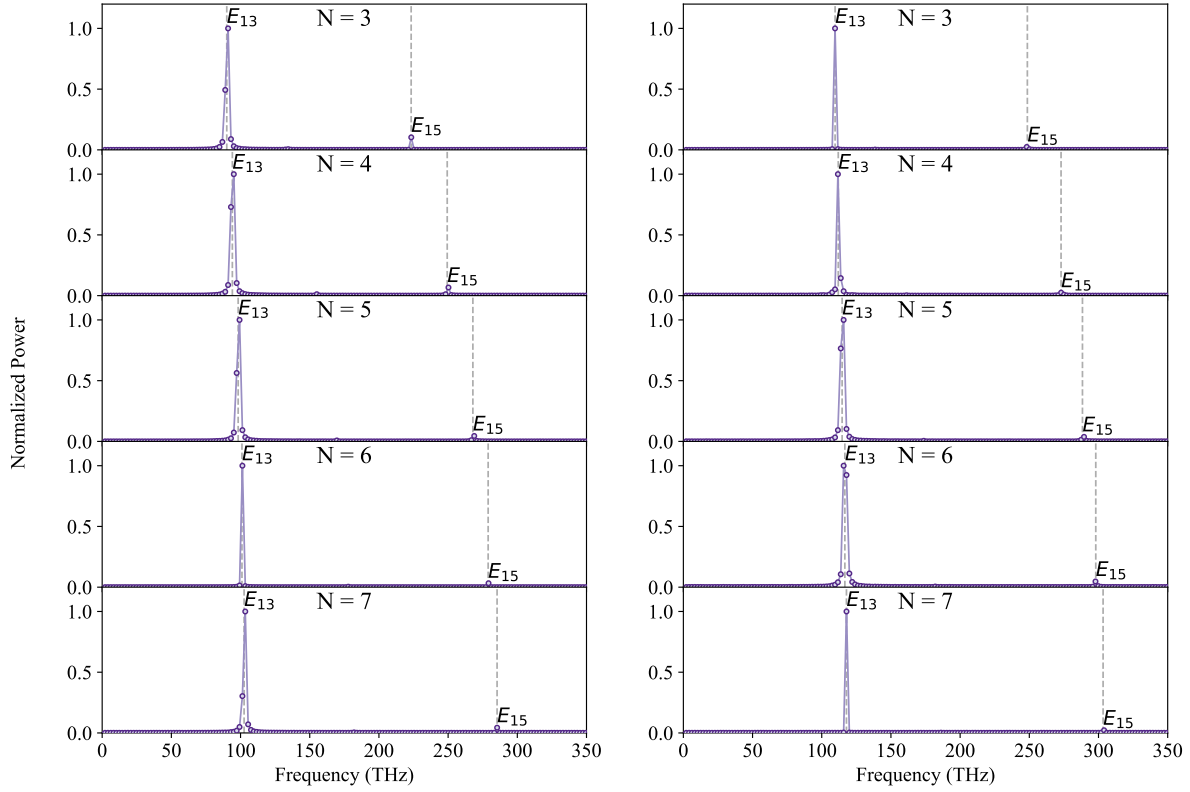


FIG. SI-6. The Fourier spectra showing all possible vibrational frequencies (as in equation SI-6) for the proton dynamics in the hydroxide (left) and Zundel (right) water cluster corresponding to the initial wavepacket $\psi_G(x;0)$. The peaks correspond to the Fourier spectra for the time evolution computed using the QSD method on IBM's QASM simulator. The gray dotted lines are the frequency differences computed using exact diagonalization.